

Banner appropriate to article type will appear here in typeset article

Exploring the Weber dependency of jet fragmentation: a Direct Numerical Simulation investigation

Romain Vallon[†], Malek Abid and Fabien Anselmet¹

¹Aix Marseille University, CNRS, Centrale Méditerranée, IRPHE, Marseille, France

(Received xx; revised xx; accepted xx)

Jet fragmentation is investigated through a Direct Numerical Simulation campaign using Basilisk (Popinet & collaborators 2013). The simulations span over one order of magnitude of gaseous Weber numbers (13 to 165), i.e. over the second wind-induced and atomization regimes, and the jets develop over distances up to 28 nozzle diameters. The study focuses on the size and velocity distributions of droplets, as well as their joint distribution. Two models derived from different theoretical backgrounds, the statistical description of the turbulence intermittency (Novikov & Dommermuth 1997) and the empirical description of the ligament-mediated fragmentation (Villermaux *et al.* 2004), are compared for describing the droplet size distribution close to the nozzle. The characteristics of the size-velocity joint distribution are explained using the vortex ring theory (Saffman 1992) which highlights two sources of fragmentation. Finally, the joint histogram of the particulate Reynolds and Ohnesorge numbers is analysed and a normalisation is suggested. It reveals that the delimitations of the droplet phase space, once properly normalised, are self-similar and independent of the gaseous Weber number, both numerically and experimentally.

Key words:

1. Introduction

Jet fragmentation occurs in numerous natural mechanisms and industrial applications. It can appear in the form of an ocean or lava spray when waves crash on the shore or during volcanic eruption, yet it is more common to find this physical mechanism in medication sprays, fuel injection systems of combustion engines or agricultural sprinkling. Jet fragmentation can be a challenging configuration to be studied numerically. Fragmentation flows of high Reynolds and Weber numbers present a large diversity of scales and fluid objects whose dynamics are partly governed by the surface tension and the turbulent characteristics of the flow, which gives them a high complexity. Their Direct Numerical Simulation (DNS) requires to solve the two phase Navier Stokes equations with surface tension. A fine resolution of the interfaces is of utmost importance and can be achieved with an optimized use of computing resources

[†] Email address for correspondence: romain.vallon@centrale-marseille.fr

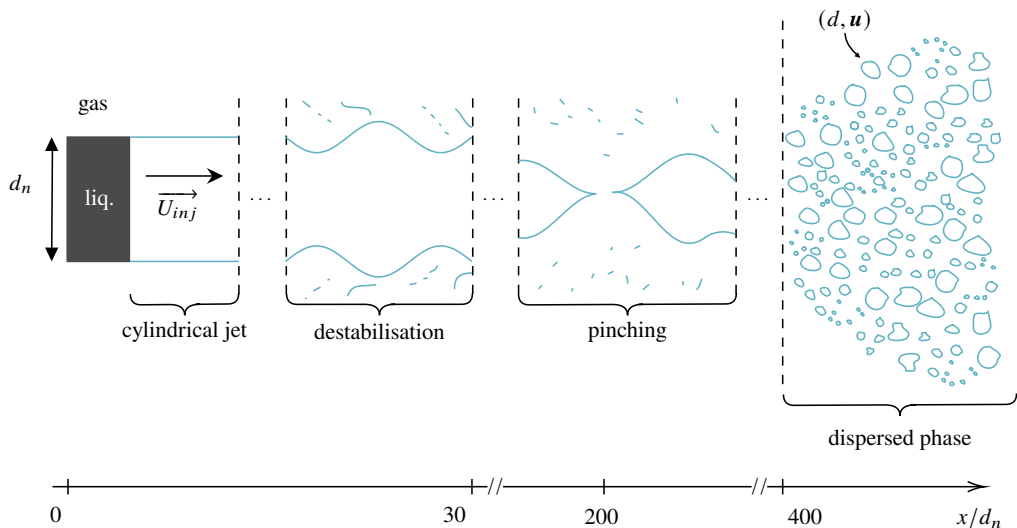


Figure 1: Scheme of the fragmentation in the second wind-induced regime of a liquid jet into a dispersed phase composed of droplets with size d and velocity vector \mathbf{u} . The distances indicated here correspond to the ones observed in the experiments of Felis *et al.* (2020), for which the jet lies in the second wind-induced regime of fragmentation with $We_2 = 24$.

thanks to adaptive grids. Those multiphase flows result from the injection of a dense phase at a velocity U_{inj} into a lighter phase through a nozzle of diameter d_n and produce a polydisperse spray. The phases are denoted by subscript i which takes the value 1 for the injected dense phase and 2 for the lighter phase. Both phases are respectively renamed liquid and gas in the following. With the Reynolds (Re) and Weber (We) numbers, the Ohnesorge (Oh) number completes the list of governing dimensionless numbers. The first one represents the ratio of inertia over viscosity and the second one the ratio of inertia over surface tension. The latter relates to the droplet deformation and represents the ratio of viscosity over the product of the surface tension and inertia. Their respective expressions follow:

$$Re_i = \frac{\rho_i U_{inj} d_n}{\mu_i}, \quad We_i = \frac{\rho_i U_{inj}^2 d_n}{\sigma}, \quad Oh_1 = \frac{\mu_1}{\sqrt{\rho_1 d_n \sigma}} \quad (1.1)$$

where ρ_i and μ_i denote the density and the dynamic viscosity of the phase i and σ the surface tension between the two phases, taken as constant.

Lefebvre & McDonell (2017) categorized five fragmentation regimes for non-assisted fragmentation of round jets, whose delimitations mainly depend on the Weber number. The focus is given here on two of them: the second wind-induced regime for which $We_2 \in [13, 40.3]$ and the so-called atomisation regime for which $We_2 > 40.3$. Complementary, the jet configurations are distinguished between large jets, $d_n > 1$ mm, and small jets, $d_n < 1$ mm. In addition, the fragmentation of a jet is often split into several breakup types: the primary and the secondary breakups. The former corresponds to the generation of elements only coming from the dense core, while the latter considers large elements dumped from the core which undergo further fragmentation, illustrated in figure 1. Thus, the physical border of the two breakup types is the location where the dense core pinches off and generates large scale elements, which are unstable in flows of moderate or large liquid Reynolds number Re_1 and gaseous Weber number We_2 .

Numerical studies of jet fragmentation mainly focus on the primary breakup region, close to the nozzle, due to limitations on computational resources and numerical challenges (Gorokhovski & Herrmann 2008; Fuster *et al.* 2009; Tryggvason *et al.* 2011; Popinet 2018). Zandian *et al.* (2017) realised DNS to study the evolution of a planar jet and specifically focused on the development of three-dimensional instabilities. Ling *et al.* (2017a) studied a quasi planar gas-liquid mixing layer at moderate density ratio ($\rho_1/\rho_2 = 20$, $Re_1 = 160000$, $We_2 = 20$) thanks to finely resolved DNS. They were able to explain precisely the development of instabilities on the sheet interface. They captured the development of Taylor Culick instabilities (Taylor 1959; Culick 1960) as well as the fragmentation of a ligament into droplets and finally compared the droplet size distribution obtained for different grid refinements with the logarithmic normal and Γ laws.

On the side of round liquid jets, the latest studies rely on DNS using the code Basilisk (Popinet & collaborators 2013) or the SPH method. Chaussonnet *et al.* (2018) used the latter to explore the droplet population produced by a twin-fluid atomizer at high pressure up to $x/d_n \approx 10$ ($\rho_1/\rho_2 = 93$, $Re_1 = 1.27 \times 10^7$, $We_2 = 1375$). Ling *et al.* (2017b) used Basilisk to observe the influence of viscosity on the fragmentation of a round biodiesel jet ($\rho_1/\rho_2 = 78.2$, $Re_1 = 1450$, $We_2 = 12.9$) developing up to $x/d_n \approx 20$ while testing different grid refinements. Zhang *et al.* (2020) observed the fragmentation of a round diesel jet injected through a solid G-spray injector, developing up to $x/d_n \approx 20$ as well ($\rho_1/\rho_2 = 233$, $Re_1 = 13400$, $We_2 = 177$). Through their study, the authors were able to observe the fragmentation of the liquid core into droplets as well as the spatial distribution of the vortices along the core. In addition, the authors modeled the droplet size distribution relative to the azimuthal angle by a hyperbolic tangent function. Finally, both studies relying on Basilisk compared the logarithmic stable and the Γ laws, the former being derived in the context of turbulence (Novikov 1994; Novikov & Dommermuth 1997) and the latter in the context of ligament mediated fragmentation (Villermaux *et al.* 2004; Villermaux 2020), to fit the droplet size distribution and concluded on the better performance of the fit with the logarithmic normal law in linear mode, i.e. fitting the signal as it is.

Later experimental studies (Stevenin *et al.* 2016; Felis *et al.* 2020) used specific droplet tracking velocimetry (DTV) and laser Doppler velocimetry (LDV) apparatus to explore the dispersed zone of agricultural-like jets ($\rho_1/\rho_2 = 828.5$, $Re_1 = 41833$, $We_2 = 24$). The measurements were carried far away from the nozzle, $x \geq 400 d_n$, in the zone where the liquid core is fully atomized and where only the secondary breakup occurs. Based on those joint size-velocity measurements, Vallon *et al.* (2021) highlighted the multimodal nature of the droplet size distribution along with the existence of droplet subgroups, each of them being characterised by a specific pair of size and velocity.

The present paper aims to complete the experimental campaigns by studying numerically the field close to the nozzle in similar flow conditions up to $x/d_n = 28$ in order to have a more global view of the fragmentation process that agricultural like jets undergo as well as to compare the logarithmic and Γ laws for describing the droplet size distribution. To do so, section 2 presents the flow modeling and the parameter framing. Section 3 is dedicated to the analysis of the overall flow characteristics. Section 4 focuses on the analysis of the droplet population statistics and the mechanisms from which they are generated, while section 5 puts in perspective the conclusions and opens up on the study of the droplet topography.

2. Flow modeling and parameter framing

This section presents the governing equations, the numerical methods, the choice of the physical configurations, the numerical configuration and the computation cost. It finally

introduces the selection of the most unstable mode of the jet, in order to stimulate the jet fragmentation.

2.1. Governing equations

Direct Numerical Simulations (DNS) aim to resolve all time and length scales by solving the Navier-Stokes equations. However, this resolution is often limited by the available computational resources. The fragmentation mechanism under consideration occurs at low Mach numbers neglecting gravitational forces and involves two immiscible, incompressible fluids. The flow dynamics is then governed by the unsteady Navier-Stokes equations and can be expressed in the theoretical framework of a one fluid flow with variable density and viscosity as:

$$\frac{\partial \rho \mathbf{u}}{\partial t} + (\mathbf{u} \cdot \nabla)(\rho \mathbf{u}) = -\nabla p + \nabla \cdot (\mu(\nabla \mathbf{u} + \nabla^T \mathbf{u})) + \mathbf{T}_\sigma \quad (2.1)$$

$$\frac{\partial \rho}{\partial t} + \nabla \cdot (\rho \mathbf{u}) = 0, \quad (2.2)$$

$$\nabla \cdot \mathbf{u} = 0 \quad (2.3)$$

where \mathbf{u} is the velocity vector, p the pressure and \mathbf{T}_σ the surface tension force, only defined on the liquid-gas interfaces. The two phases are taken into account in the one fluid framework through the phase indicator, named fraction field and denoted α in the following. The fraction equals 1 if a cell only contains liquid and 0 if it only contains gas. The one fluid viscosity and density are computed over the phase quantities following $\mu = \alpha\mu_1 + (1 - \alpha)\mu_2$ and $\rho = \alpha\rho_1 + (1 - \alpha)\rho_2$. Injecting the expression of ρ and μ in Eq. 2.2 and noting that $\partial_t \rho_1 = \partial_t \rho_2 = 0$ lead to reformulate the continuity equation in terms of α :

$$\partial_t \alpha + \nabla \cdot (\alpha \mathbf{u}) = 0 \quad (2.4)$$

which can also be seen as the advection equation of the volume fraction. Instead of resolving the Navier Stokes equations for each phase, this approach enables the resolution of only a single set of equations. This, though, implies the implicit assumption that the velocity field \mathbf{u} evolves continuously in space.

2.2. Numerical methods

The DNS under consideration are computed with the solver developed by the Basilisk community. Basilisk is an open source project which aims to develop efficient solvers and methods which can be adapted to a wide range of configurations (Popinet & collaborators 2016). This project is mainly led by Stéphane Popinet and benefits from the contribution of all the Basilisk community. The present study largely relies on the atomisation code available on the wiki of the project (Popinet & collaborators 2016).

The Navier-Stokes equations are solved for a biphasic flow with a constant surface tension using numerical schemes similar to those of Popinet (2003) and Lagrée *et al.* (2011). The resolution of the equations relies on time steps limited by the Courant-Friedrichs-Lewy (CFL) condition, the advection scheme of Bell-Collella-Glaz (Bell *et al.* 1989) and an implicit solver for the viscosity. The gas-liquid interface is tracked with a Volume-Of-Fluid (VOF) scheme which is geometric, conservative and non-diffusive (López-Herrera *et al.* 2015). Regarding the surface tension, the interfacial force is calculated as $\mathbf{T}_\sigma = \sigma \kappa \mathbf{n} \delta_s$, where κ is the interface curvature, δ_s is the interface Dirac function and \mathbf{n} is the normal vector to the interface pointing outward. Considering the Continuum-Surface-Force (CSF) method

and the Peskin immersed boundary method, the interfacial force can be approximated by $\mathbf{T}_\sigma = \sigma \kappa \nabla \alpha$ where κ is computed by the use of a height function (Abu-Al-Saud *et al.* 2018). A projection method is used to compute the centered pressure gradient and the acceleration field. The VOF scheme is combined with an octree adaptive grid (Agbaglah *et al.* 2011) while the grid adaptation algorithm relies on a wavelet estimated discretization error, described by Popinet (2015) and used for atmospheric boundary layer simulations by van Hooft *et al.* (2018). Such grids present the advantage of finely resolving the gas-liquid interface while having a coarser resolution away from the interfaces, and thus decreasing the time needed for computing the DNS. Finally, the droplet detection is achieved by a tag function which associates a different tag to each neighbourhood of connected cells respecting a threshold condition on the fraction field, set to $\alpha > 1 \times 10^{-3}$ in our DNS.

2.3. Physical configuration and parameters

The domain is a cubic box of dimension L_x . A liquid round jet is injected into a quiescent gas at a mean velocity U_{inj} , directed along the x -axis, through a disc of diameter d_n and length $l_x = d_n/3.2$. The latter disc is called nozzle in the following. The injection condition is set on the disc face located at $x = 0$ while a free stream condition is imposed at the location $x = L_x$. In addition, a Neumann condition on the normal velocity is imposed on the lateral faces. A sinusoidal perturbation is superimposed on the injection velocity in order to accelerate the development of the Kelvin Helmholtz instability on the interface. The perturbation has an amplitude A and a frequency f such that the injection velocity follows $u_{inj} = U_{inj}(1 + A \sin(2\pi ft))$. Finally, the advection timescale is defined by $T_a = d_n/U_{inj}$.

One aim of this study is to draw comparisons with the experiments of Felis *et al.* (2020). First and foremost, the turbulent property of the experimental inlet velocity profile is let aside and the numerical injection profile is set as laminar. Real world parameter values cannot be picked because the current computational resources do not allow to compute such configurations. For instance, the numerical constraints prohibit large values for the density ratio, $\rho_1/\rho_2 < 200$, the Reynolds number, $\max(Re) = O(10^4)$ and the surface tension, $\sigma = O(10^{-5})\text{N/m}$. Those constraints are denoted C_0 , C_1 and C_2 . Even if the real world values are unreachable, a specific attention can be set on reproducing configurations with dimensionless numbers close to the experimental ones. The latter study carried out DTV and LDV measurements on a water jet lying in the second wind-induced fragmentation regime (Lefebvre & McDonnell 2017). This regime is characterised by sharp limits on the gas Weber number: $13 < We_2 < 40.3$. The atomisation regime is also defined on the basis of the Weber number, $We_2 > 40.3$. The first priority is thus to make the DNS Weber numbers evolve over this range of values, which defines a third constraint, C_3 . In order to reproduce similar deformation regimes undergone by the droplets, considering the Ohnesorge number is relevant. Experimentally, $Oh_1 = 3.4 \times 10^{-3}$, reproducing the same order of values makes a fourth constraint C_4 . Having a density ratio of $O(10^3)$, as for water injection in air, is impossible. Conserving the experimental viscosity ratio $\nu_2/\nu_1 = 15$ could be interesting but it would slow down the fragmentation process, which goes against the optimisation of computer resources. One could then have a look at the conservation of the ratio $\gamma = \mu_1/\mu_2 = (\rho_1\nu_1)/(\rho_2\nu_2)$, where it is worth noting that the quantity $\rho_i\nu_i d_n$ is homogeneous to a mass flow rate \dagger . Furthermore, γ rewrites as $\rho_1\rho_2^{-1}/(\nu_2\nu_1^{-1}) = We_1We_2^{-1}/(Re_1Re_2^{-1}) = We_1Re_1^{-1}/(We_2Re_2^{-1}) = Ca_1/Ca_2$, where Ca_i is the Capillary number of the phase i . Experimentally, γ equals 55 and can be seen such that the mass flow rate of the liquid phase is 55 times higher than the mass flow rate of the gas phase, or equivalently $Ca_1 = 55Ca_2$.

\dagger Indeed, $[\rho_i\nu_i d_n] = \frac{\text{kg}}{\text{m}^3} \times \frac{\text{m}^2}{\text{s}} \times \text{m} = \text{kg} \times \text{s}^{-1}$. Also, $\rho_i\nu_i d_n = \rho_i U_{inj} d_n^2 / Re_i$.

ρ_1 (kg/m ³)	ρ_2 (kg/m ³)	ν_1 (m ² /s)	ν_2 (m ² /s)	σ (N/m)	d_n (m)	Oh_1
1	1/55	10 ⁻⁶	10 ⁻⁶	10 ⁻⁵	4.48 × 10 ⁻³	4.725 × 10 ⁻³

Table 1: Fixed parameters and the corresponding Ohnesorge number.

DNS	U_{inj} (m/s)	We_2	Re_1	f (kHz)	St	DNS	U_{inj} (m/s)	We_2	Re_1	f (kHz)	St
1	1.357	15	6079	0.340	1.12	6	2.216	40	9928	0.901	1.82
2	1.567	20	7020	0.454	1.30	7	3.0	73.3	13440	1.666	2.49
3	1.787	26	8004	0.587	1.47	8	3.5	99.8	15680	2.272	2.91
4	1.919	30	8598	0.676	1.58	9	4.0	130.3	17920	2.972	3.33
5	2.073	35	9287	0.795	1.72	10	4.5	165	20160	3.730	3.71

Table 2: Injection velocities and corresponding gas Weber and liquid Reynolds numbers along with the frequency f of the most unstable mode and the corresponding forcing Strouhal number St .

Respecting this ratio makes a fifth constraint C_5 . The list of constraints necessary to produce configurations close to the experiments is thus:

$$\left\{ \begin{array}{l} C_0 : \rho_1/\rho_2 < 200 \\ C_1 : \max(Re) = O(10^4) \\ C_2 : \sigma = O(10^{-5}) \text{ N/m} \end{array} \right. \quad \& \quad \left\{ \begin{array}{l} C_3 : We_2 \in [13, 40.3] \text{ or } We_2 > 40.3 \\ C_4 : Oh_1 = O(10^{-3}) \\ C_5 : \rho_1 \nu_1 / \rho_2 \nu_2 = 55 \end{array} \right. \quad (2.5)$$

which let the parameters ρ_1 , ρ_2 , ν_1 , σ , U_{inj} and d_n free to choose. In order to keep a constant geometry between different DNS, the nozzle diameter is set as constant and only the injection velocity varies to cover the range of Weber and Reynolds of interest. Table 1 gives the values chosen for the parameters along with the corresponding Ohnesorge number. Table 2 lists the chosen injection velocities and the corresponding gaseous Weber and liquid Reynolds numbers. Note that the Ohnesorge number is constant over all the configurations. Thus, for all the DNS, the critical breakup Weber number for a given droplet size is constant (Hinze 1955). Additionally, the breakup regimes in the secondary atomisation are defined on the same range of Weber numbers (Faeth *et al.* 1995) for the 10 DNS. *In fine*, the breakup regimes of the droplets are set and identical for any pair (Re_1, We_1) and the DNS explore different breakup regimes of the jet by ranging from low to moderate Re and We numbers.

2.4. Most unstable mode for triggering the jet fragmentation

In order to trigger the jet fragmentation the earliest and save computational resources, it is worth destabilizing the jet interface. Following the work of Yang (1992) on the growth of waves in round jets, it is possible to characterise the most unstable axisymmetric mode. In this work, the author studied the stability of an infinitesimal perturbation on the surface of a round jet of radius a and derived the expression of the nondimensional temporal growth rate for the m -th transversal mode, $(\alpha_r^*)_m^2$. This derivation is recalled in appendix A.

Figure 2a gives the evolution of this nondimensional growth rate for an axisymmetric perturbation, selected with $m = 0$, $U_{inj} = 3.0$ m/s and a zero gas velocity injection. The wavelength ka of the most unstable mode is such that $(\alpha_r^*)_m^2$ is maximum. The mode

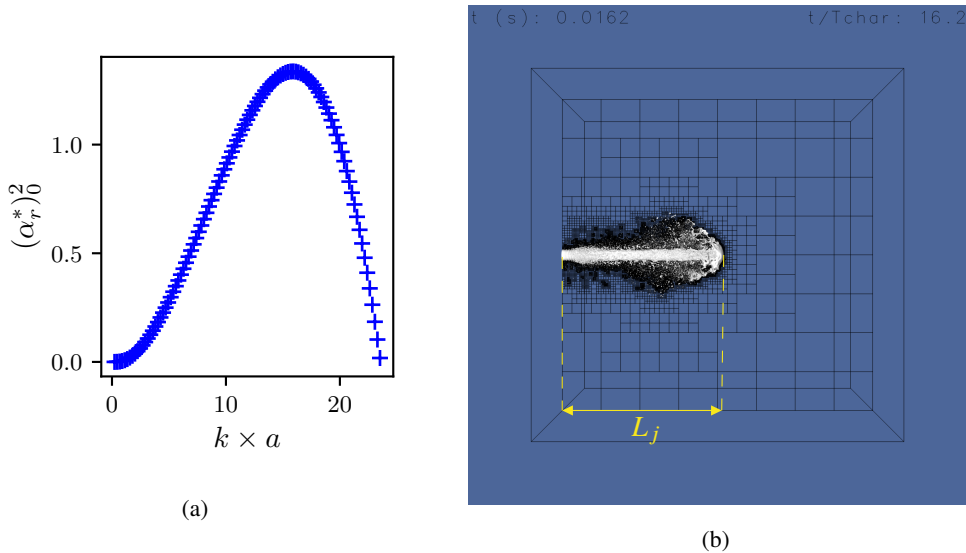


Figure 2: (a) Evolution of the nondimensional temporal growth rate $(\alpha_r^*)^2$ for $U_{inj} = 3.0$ m/s. (b) Atomisation and adaptive grid for $We_2 = 165$ (DNS 10) at $t/T_a = 16.2$.

pulsation ω is then given by the imaginary part of the growth rate. During the computation, a was set to d_n instead of $d_n/2$. The difference between the pulsation of the mode computed for $a = d_n$ and $a = d_n/2$ is of $O(1\text{rad/s})$ while the pulsations are of $O(10^3\text{rad/s})$. The relative difference is thus of $O(10^{-3})$, which seems acceptable to the authors. Table 2 lists the most unstable mode frequencies f for each configuration defined in section 2.3 as well as the Strouhal number based on the forcing frequency, $St = f \times d_n/U_{inj}$.

2.5. Numerical configuration and computational cost

The refinement level is set to 12 and the minimum cell size in an adaptive grid is given by $\Delta_{min} = L_x/2^{12}$. Hence the minimum cell size is $\Delta_{min} = 30.5 \mu\text{m}$ and $d_n/\Delta_{min} = 146.8$. The time step is set by the CFL condition, $|u_{max}|\Delta t/\Delta_{min} < C$, where the Courant number is initially set to 0.8. Running the 10 DNS summed a total of 511 896 scalar hours of computation. Each of the DNS 3 to 10 ran for 60 480 h while DNS 1 and 2 respectively ran for 12 600 h and 15 456 h. The computational performances can be tracked by checking the total number of cells used for each DNS, C_{tot} , the mean numerical velocity, $\overline{V_{num}}$, the maximal physical time reached by the simulations, t_{max}/T_a , the maximum jet elongation, $L_{j,max}/d_n$ and the total number of detected droplets, N_{tot} . The latter three are summarized in table 3 while the other performances parameters are given in appendix B. All the DNS are split into 3 runs and were computed in parallel on the Occigen HPC (CINES, France), typically on 840 cores. An example of atomisation produced at $We_2 = 165$ (DNS 10) is given in figure 2b.

3. Overall flow characteristics and droplet statistics

This section characterises the Turbulent Kinetic Energy (TKE) in the domain, has a glance on the jet interface and introduces the statistics and PDFs of the droplet population. In the following, the evolution of several variables relatively to t/T_a is analysed.

DNS	We_2	t_{max}/T_a	$L_{j,max}/d_n$	N_{tot}	DNS	We_2	t_{max}/T_a	$L_{j,max}/d_n$	N_{tot}
1	15	34	28	70	6	40	34	28	3545
2	20	34	28	459	7	73.3	24.2	21.5	9725
3	26	34	28	1949	8	99.8	19.75	17.0	18478
4	30	34	28	2182	9	130.3	18.5	14.4	32922
5	35	34	28	2448	10	165	16.25	14.2	45046

Table 3: Maximum normalised time t_{max}/T_a along with the corresponding normalised maximum jet elongation $L_{j,max}/d_n$ and total number of droplets N_{tot} .

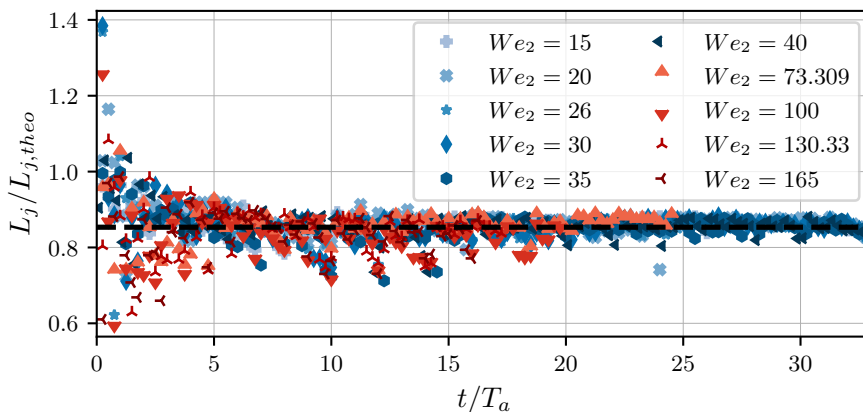


Figure 3: Color on-line. Temporal evolution of the jet length L_j compared to the theoretical jet length $L_{j,theo}$ for the 10 DNS. The black dashed line represents the mean value $L_{jet,max}/L_{jet,theo} = 0.853$ averaged over $t/T_a \in [0, 33]$. The blue colours denote the DNS in the second wind-induced regime and the red colours the DNS in the atomisation regime.

If the liquid core motion was the one of a solid cylinder, then the jet length would theoretically be $L_{j,theo} = d_n \times t/T_a$, i.e. $L_{j,theo}/d_n = t/T_a$. However, a lag of the jet tip relatively to this theoretical position is observed. In order to link t/T_a and the actual jet length L_j , figure 3 gives the temporal evolution of $L_j/L_{j,theo}$. Here, L_j is defined as the 99% quartile of the axial positions of the interface cells, $\alpha \in]0, 1[$, and not the maximum position. Doing so enables to exclude liquid cells which would exist on the upstream face of the jet tip as well as to smooth out the effect of the grid refinement. Thus, the length of the jet equals in average 85% of the theoretical length, $L_j/d_n \approx 0.85 \times t/T_a$, and the velocity of the jet front equals $0.85 U_{inj}$. Note as well that $t/T_a = 33$ corresponds to the instant when the jet exits the computational domain.

3.1. Turbulent kinetic energy

One aim of this study is to draw conclusions on the statistics of the droplet population. To ensure converged statistics, the flow needs to reach a statistically steady state. Looking at the turbulent kinetic energy k_i enables to conclude on this, primarily the one of the gas phase. As shown in Table 3, the jet extension observed for $We_2 \in [73, 165]$ (DNS 7 to 10) is smaller than the length L_x of the domain. Thus, a statistically steady state at the scale of the domain

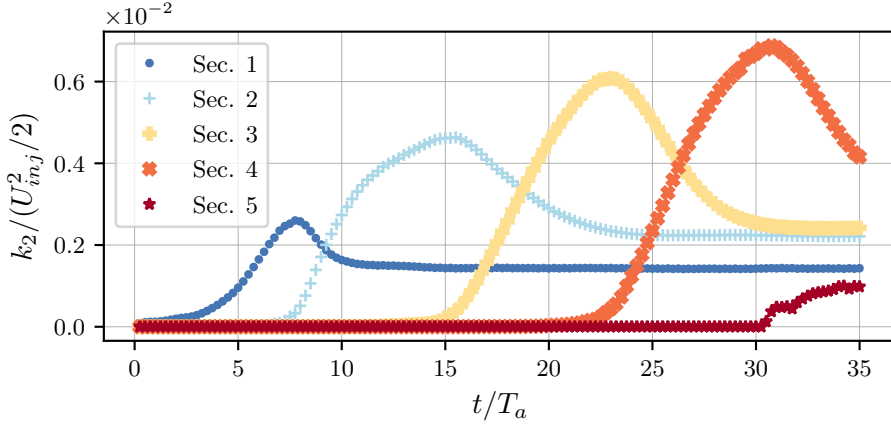


Figure 4: Turbulent kinetic energy in the gas phase for $We_2 = 40$ (DNS 6).

cannot be achieved. Even so, it is possible to slice the domain in different sections along the x -axis and conclude on the flow steadiness in each section.

The domain of length L_x is sliced in 5 sections along the x -axis. The fifth section represents the outlet side of the domain and its length is set to d_n . The rest of the domain is evenly sliced with a slice thickness equal to $(L_x - d_n)/4$. The sections are denoted from 1 to 5, going from the nozzle to the outlet face. The turbulent kinetic energy is computed for both the gas and the liquid following $k_i = \frac{1}{2} \int_{V_s} (u'_{x,i}{}^2 + u'_{y,i}{}^2 + u'_{z,i}{}^2) dV$ with V_s the volume of the section under consideration. Figure 4 shows the time evolution of the TKE for $We_2 = 40$ (DNS 6). The evolution is similar in each slice: k increases when the jet head enters the section, reaches a maximum, decreases when the head enters the following section and finally reaches a plateau. The time sampling is set with a step $\Delta(t/T_a) = 1/4$ and smooths the fluctuations out of the plateau region. The increase of the k_2 maximum and asymptote values between the slices is due to the ongoing fragmentation and the newly created droplets, which increases the agitation of the gas phase. Thus, once the jet head fully exits a section, the flow reaches a statistically steady state. One could expect that the TKE around the jet head, measured from a Lagrangian point of view, would reach an asymptote as well and, thus, a statistically steady state.

3.2. Close up on the jet interface

This section explores qualitatively the interface of the jet in two regions of interest: close to the nozzle where the unstable mode develops and around the tip of the jet where the front extends and fragments.

3.2.1. Development of the unstable mode

In order to check qualitatively the forcing implemented in the simulations and its outcome, one could have a look on the jet interface in the region of the nozzle, where the unstable mode excited by the forcing should develop. To compare the interface evolution between the different DNS, the x coordinate needs to be normalised by the characteristic length scale of the forcing, i.e. $U_{inj} f^{-1}$. Note here that $U_{inj} f^{-1} = St/d_n$, so $x/(U_{inj} f^{-1}) = (x/d_n)St$, where St is the Strouhal number based on the forcing, given in Table 2. Furthermore, the physical times chosen for the comparison have to be in phase relatively to the sinusoidal perturbation, i.e. the physical times should be chosen such that the perturbation waves superimpose on

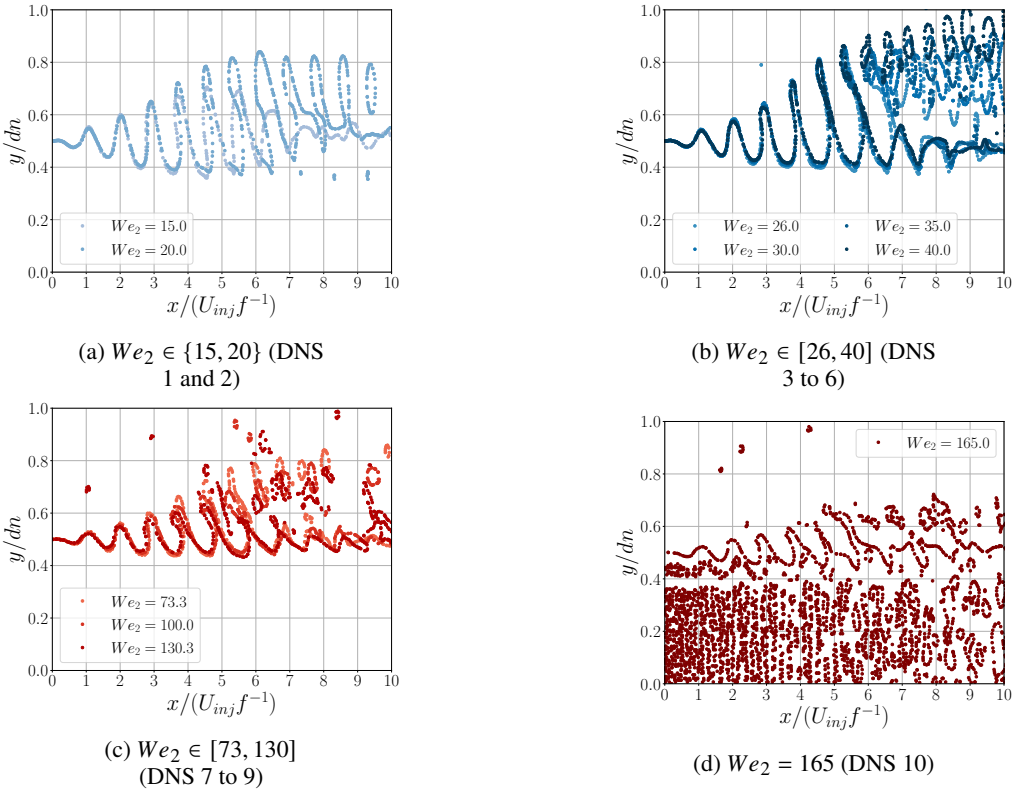


Figure 5: Color on-line. Superposition of the interface sliced at $z = 0$ in the region of the nozzle in the second wind-induced regime (a,b) and the atomisation regime (c,d). The blue and red colors indicate the second wind-induced and atomisation regimes, respectively. The physical times are chosen such that the sinusoidal perturbations are in phase. As a reminder, $x/(U_{inj} f^{-1}) = (x/d_n)St$.

each other. Figure 5 shows the jet interface sliced at $z = 0$ and for $y/d_n > 0$, normalised as explained.

For the 10 DNS, the perturbation waves collapse well after normalising by $U_{inj} f^{-1}$ and picking in-phase physical times. Consider first the second wind-induced regime. The jet interfaces for $We_2 \in \{15, 20\}$ (DNS 1 and 2) are represented separately from those for $We_2 \in [26, 40]$ (DNS 3 to 6), figure 5a and 5b, to highlight the different behavior of the forcing between them, even if DNS 1 to 6 lie in the second wind-induced regime. For the DNS 1 and 2, the development of the mode leads to waves which only break in large elements in the latter, while they are attenuated in the former. Contrarily, the perturbation in the DNS 3 to 6 leads to the development of shorter waves which break into a wider droplet population. Here, the wave develops in the radial direction. While the wave extends radially, up to $y/d_n \approx 0.8$, its outskirts forms a rim and the space between the liquid core and the outer rim forms a sheet. The sheet becomes thinner the more the wave extends, before fragmenting for $x/(U_{inj} f^{-1}) \in [5.5, 7]$. Once the sheet has fragmented, the rim destabilizes and fragments as well. A similar wave development can be observed for $We_2 \in [73, 130]$ (DNS 7 to 9), except that the wave extension is smaller than previously, up to $y/d_n \approx 0.6$, that the wave sheet fragments earlier, for $x/(U_{inj} f^{-1}) \in [5, 6]$, and that the rim fragments faster for DNS 7 or even hardly exists for DNS 8 and 9. Finally, no rim is created when $We_2 = 130$ (DNS 9). Specific attention is required for $We_2 = 165$ (DNS 10). Figure 5d indicates the presence

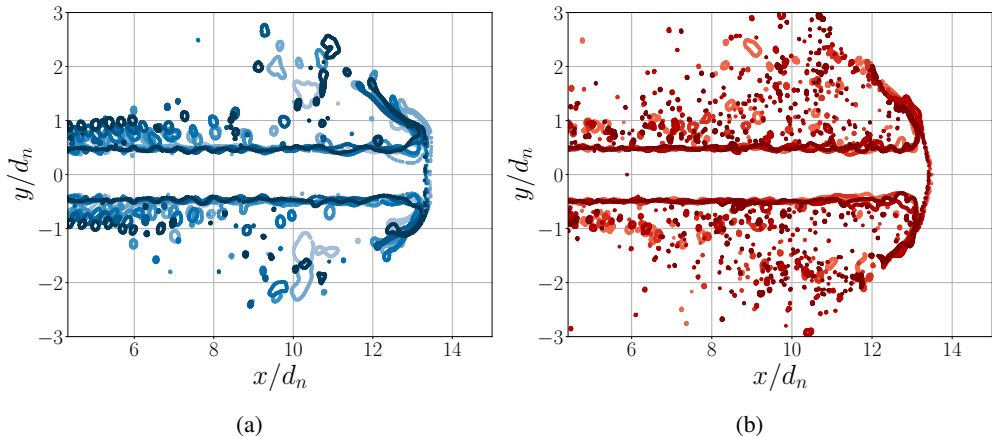


Figure 6: Color on-line. Superposition of the interface sliced at $z = 0$ in the region of the jet head in the second wind-induced regime (a) and in the atomisation regime (b) at $t/T_a = 15$.

of interface in the liquid core, meaning that the core is populated by some volume made of the lighter phase, i.e. bubbles. The “bubbles” are generated from $t/T_a \approx 10$ and are likely to originate from a numerical artefact related to the volume fraction threshold used for droplet detection. Note that bubbles also appear, but later on timewise, in the DNS 9. The presence of bubbles changes the fluid dynamics inside the core but appears to modify only slightly the interface dynamics in the time scope of the study and any perturbation would be smoothed out by considering the overall droplet population.

3.2.2. Development of the jet head

In addition to the development of the wave perturbation, it is possible to have a glance on the head of the jet. Figure 6 presents the jet interface sliced at $z = 0$ in the region of the head of the jet for both regimes at the same physical time, $t/T_a = 15$. What appears at first is the difference of geometry of the front between the two regimes. In the second wind-induced regime, the front is plane while it is parabolic in the atomisation regime. This difference results from the force equilibrium between the liquid and gas phases depending on the injection velocity. In both regimes, the head extends up to $y/d_n \approx 2$ and experiences piercing (data not shown here) which could be due to the Taylor Culick instability (Taylor 1959; Culick 1960). However, the dynamics of the head extension is quite different. In the second wind-induced regime, the head extension can produce thick ligaments able to extend over distances of the order of d_n while, in the atomisation regime, the ligaments fragment once they are detached from the head sheet. The difference in the resulting droplet population is qualitatively visible in figure 6 where the droplets appear to be more numerous in the atomisation regime than in the second wind-induced regime.

3.3. Statistics of the droplet population

Figure 7 presents the evolution of N_{tot} , the number of droplets detected by the tag function implemented in Basilisk. First and foremost, the droplets produced for $We_2 \in \{15, 20\}$ (DNS 1 and 2) do not exceed 1000 elements, which is not enough to draw conclusions on the statistics of those two populations. Thus, the DNS 1 and 2 are discarded in the following. All the other DNS show a total number of elements larger than 1000, which enable to carry out a statistical analysis. The two regimes distinguish from each other by the total

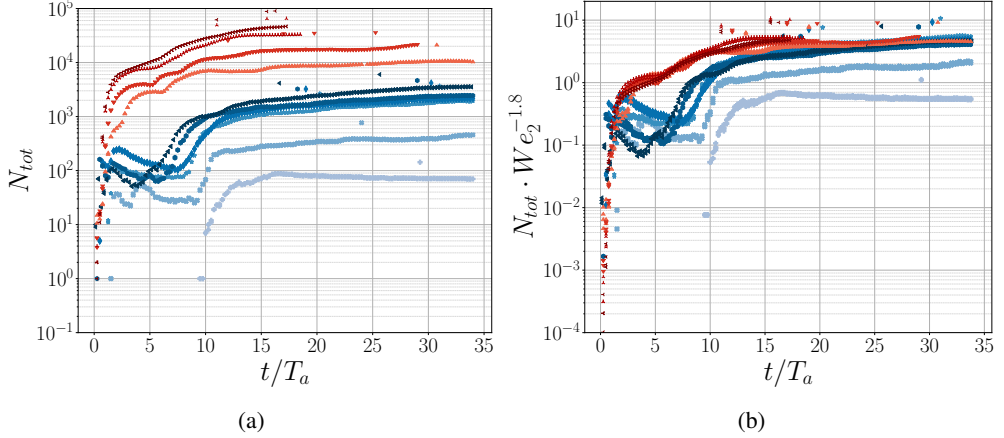


Figure 7: Total number of detected droplets, (a) unscaled and (b) scaled by $We_2^{-1.8}$. The blue and red colours denote the second wind-induced and atomisation regimes. The color code denoting the DNS is the same as in Figure 3.

number of produced droplets. The total number is of $O(10^3)$ in the second wind-induced regime whereas it is of $O(10^4)$ in the atomisation regime, reaching up to 5×10^4 elements for $We_2 = 165$ (DNS 10). Even so, after rescaling by $We_2^{1.8}$, the numbers of elements for $We_2 \in [26, 165]$ (DNS 3 to 10) collapse all together and N_{tot} tends toward $5 We_2^{1.8}$ for both regimes, excepted DNS 1 and 2. The transition to a steady production of droplets differs between the two regimes. In the second wind-induced regime, the total number of elements quickly increases and drops before reaching a steady rate. The observed decrease could be due to the interactions between the jet head development and the corollas induced by the mode forcing, interactions which bring the droplets back to the liquid core. All the 10 DNS are close to a steady regime with a slight departure because of the difference in the maximum physical time reached by each DNS. The temporal evolution of the mean value for the size, axial and radial velocity as well as a proposal of scaling are given in appendix D.

The arithmetic mean operator and the standard deviation are respectively denoted $\langle \cdot \rangle$ and σ while the skewness and the excess kurtosis are respectively denoted S and κ . Here, we considered the excess kurtosis equal to the kurtosis subtracted by 3 such that the normal distribution has a zero excess kurtosis. Figure 8 gives the evolution along We_2 of the four first statistical moments along with the minimum and the maximum values for the size at the time instants $t/T_a = 15$ and $t/T_a = 25$. Note that the droplet tagging function implemented in Basilisk can return droplets with a volume V smaller than Δ_{min}^3 , the volume of the smallest grid cell. This behavior is expected and due to the cells having a volume fraction f between 10^{-3} and 1 and being disconnected from any liquid neighbourhood. To ensure physical consistency regarding the grid characteristics, all the droplets with a volume smaller than or equal to the minimum cell volume are discarded, i.e. any droplets such that $V \leq \Delta_{min}^3$. Assuming spherical droplets, this condition implies a minimum droplet diameter $d_{min} = \sqrt[3]{6/\pi} \Delta_{min} \approx 37.8 \mu\text{m}$.

Let us consider the statistical moments of the droplet size. Details about the evolution of the moments for the axial and radial velocities are given in appendix E. Globally, both the mean and standard deviation decrease with We_2 and are of $O(100 \mu\text{m})$. Similarly, the maximum value decreases but is one order larger, $O(1 \text{ mm})$. Meanwhile, the skewness and the excess kurtosis slightly increase and are respectively of $O(1)$ and $O(10)$. An increase in We_2 corresponds to an increase of the inertial forces relatively to the surface tension forces.

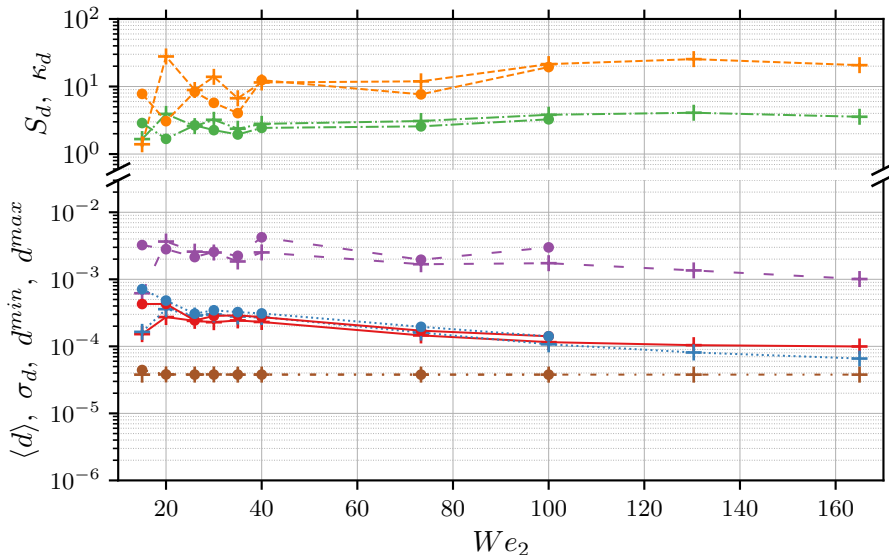


Figure 8: Color on-line. Evolution of $\langle \cdot \rangle$ (red), σ (blue), S (green), κ (orange), the minimum (purple) and maximum (brown) against We_2 for the size d . The pluses (+) correspond to $t/T_a = 15$ and the bullets (•) to $t/T_a = 25$. Note that S and κ are both dimensionless and that the dimensional variables are expressed with the SI base units.

Then, the larger We_2 , the more likely the droplets undergo fragmentation and fewer sizes are stable. Thus, the mean diameter and the maximum diameter decrease and more droplets group around the mean diameter which, as a consequence, reduces the standard deviation. A decrease of the minimum diameter should also occur, but the condition on the minimal droplet volume numerically filters out any diameter smaller than $37.8 \mu\text{m}$. In parallel, the increase in the skewness value, which is positive, points out that the droplet size distribution is slightly more right-tailed with higher We_2 . This indicates that the right-hand tail, towards sizes larger than $\langle d \rangle$, exists on a size range larger than the one on which the left-hand tail exists. Finally, the positive sign and the increase of the excess kurtosis with We_2 indicates that the distributions are leptokurtic for all the values of We_2 and that the distribution tail increases in length relatively to the mean and the standard deviation. Equivalently, the range of rare very large sizes, relatively to the mean, is both broader with higher We_2 and larger than the Gaussian distribution for which $\kappa = 0$. As the flow geometry remains the same for the different values of We_2 , the increase in the excess kurtosis and the skewness is due to the depletion of large sizes in the benefits of small sizes, grouped around the mean diameter. However, even if d_{max} decreases, the large values of S and κ show that the larger droplet sizes do not disappear completely from the flow and still exist at higher values of We_2 .

Finally, the values of the skewness and the excess kurtosis of the size distribution are very large and one order of magnitude larger than those of the velocity distributions, see appendix E. This indicates a wider spanning range for the size distribution than for the two velocity distributions and justifies the use of a loglog scale to visualise the size distribution.

3.4. Distributions of the size and the velocity

Complementary to the statistical moments, it is worth looking at the distributions of the sizes and the velocities of the droplets. For the sake of clarity, the number PDF of any

DNS	We_2	λ (μm)	$\lambda/\langle d \rangle_{15}$	$\lambda/\langle d \rangle_{25}$	DNS	We_2	λ (μm)	$\lambda/\langle d \rangle_{15}$	$\lambda/\langle d \rangle_{25}$
1	15	1031	7	2.50	6	40	632	2.83	2.37
2	20	893	3.47	2.21	7	73.3	467	3.37	–
3	26	784	3.36	3.28	8	99.8	400	3.65	–
4	30	729	3.29	2.62	9	130.3	350	3.52	–
5	35	675	2.85	2.37	10	165	311	3.28	–

Table 4: Estimation of the Taylor microscale λ and its normalised values at $t/T_a = \{15, 25\}$.

variable ζ is denoted \mathcal{P}_ζ in the following. Even if the mean values of the size and the velocities are not fully converged, we consider the PDF of each variable normalised by its mean. However, u_y being close to zero in average, normalising by $\langle u_y \rangle$ is not relevant and $u_y/\langle u_x \rangle$ is considered instead. Figure 9 gives the PDFs of $d/\langle d \rangle$, $u_x/\langle u_x \rangle$ and $u_y/\langle u_x \rangle$ at the time instants $t/T_a = 15$, where both regimes are computed, and $t/T_a = 25$. First of all, it is interesting to note that the PDFs in each regime collapse for the three variables even if the mean values are not converged. From the three distributions, only that for $u_y/\langle u_x \rangle$ shows a similar behavior between the two regimes of fragmentation, excepting for the width and the slope of the tails. For both regimes, the PDF tails scale with $\exp(\pm a \times u_y/\langle u_x \rangle)$ where a nearly equals 6 in the second wind-induced regime and nearly equals 3 in the atomisation regime. The difference in the tail width goes along with the difference between the exponential coefficient. Indeed, the larger the coefficient is, the smaller the tail width is. This can be explained once again with the increase of the relative velocity between the injection and the gas phase, and thus the shear, when We_2 increases. Note that, due to the flow symmetry, $\mathcal{P}_{u_z/\langle u_x \rangle}$ follows a trend similar to that of $u_y/\langle u_x \rangle$.

Regarding the size distribution, different modes appear clearly between the two fragmentation regimes. The size PDF derived from the atomisation regime shows one main mode centered on $d/\langle d \rangle = 0.5$ while the PDF for the second wind-induced regime shows 3 modes centered on $d/\langle d \rangle = \{0.2, 1, 2.5\}$, denoted from 1 to 3 in figure 9b. Even if the main mode appears to be shifted towards larger $d/\langle d \rangle$ when We_2 increases, it refers to the same range of physical sizes d between $47 \mu\text{m}$ and $58 \mu\text{m}$ with a mean value of $55 \mu\text{m}$, considering $We_2 \in [26, 165]$ (DNS 3 to 10).

Tennekes & Lumley (1972) derived handy equations to estimate the turbulent Reynolds number Re_τ from the ratio of the extreme scales of the flow and the Taylor microscale Reynolds number Re_λ : $Re_\tau \propto (d_n/\Delta_{min})^{4/3}$ and $Re_\lambda \approx \sqrt{Re_\tau}$ where $Re_\lambda = u_{RMS}\lambda/\nu_2$ and $\Delta_{min} = 30.5 \mu\text{m}$, see section 2.5. With the chosen configuration, the estimation gives $Re_\tau \approx 775$ and $Re_\lambda \approx 27.8$. Besides, assuming that the turbulence intensity is around 20% of the injected velocity, i.e. $u_{RMS} = 0.2 U_{inj}$, it is possible to estimate the Taylor microscale λ . Table 4 lists the estimation of λ for the 10 DNS. The Taylor microscale decreases with the gaseous Weber number We_2 , which is expected as Re_λ is set by the configuration and u_{RMS} increases with the injection velocity. Physically, the root mean square velocity increases with the injection velocity and the Taylor microscale decreases. Most importantly, the normalised values of λ correspond to the third mode of $\mathcal{P}_{d/\langle d \rangle}$ at both $t/T_a = \{15, 25\}$ in the second wind-induced regime, $We_2 < 40.3$, and indicate that the larger droplets observed in the DNS might be related to the most probable vortex size set by the gas turbulence.

$\mathcal{P}_{d/\langle d \rangle}$ in both regimes shows a similar tail evolution scaling as $(d/\langle d \rangle)^{-2.7}$, which was also observed experimentally (Vallon *et al.* 2021). This power law scaling goes against the experimental observation of Simmons (1977) who remarked that the size distribution in

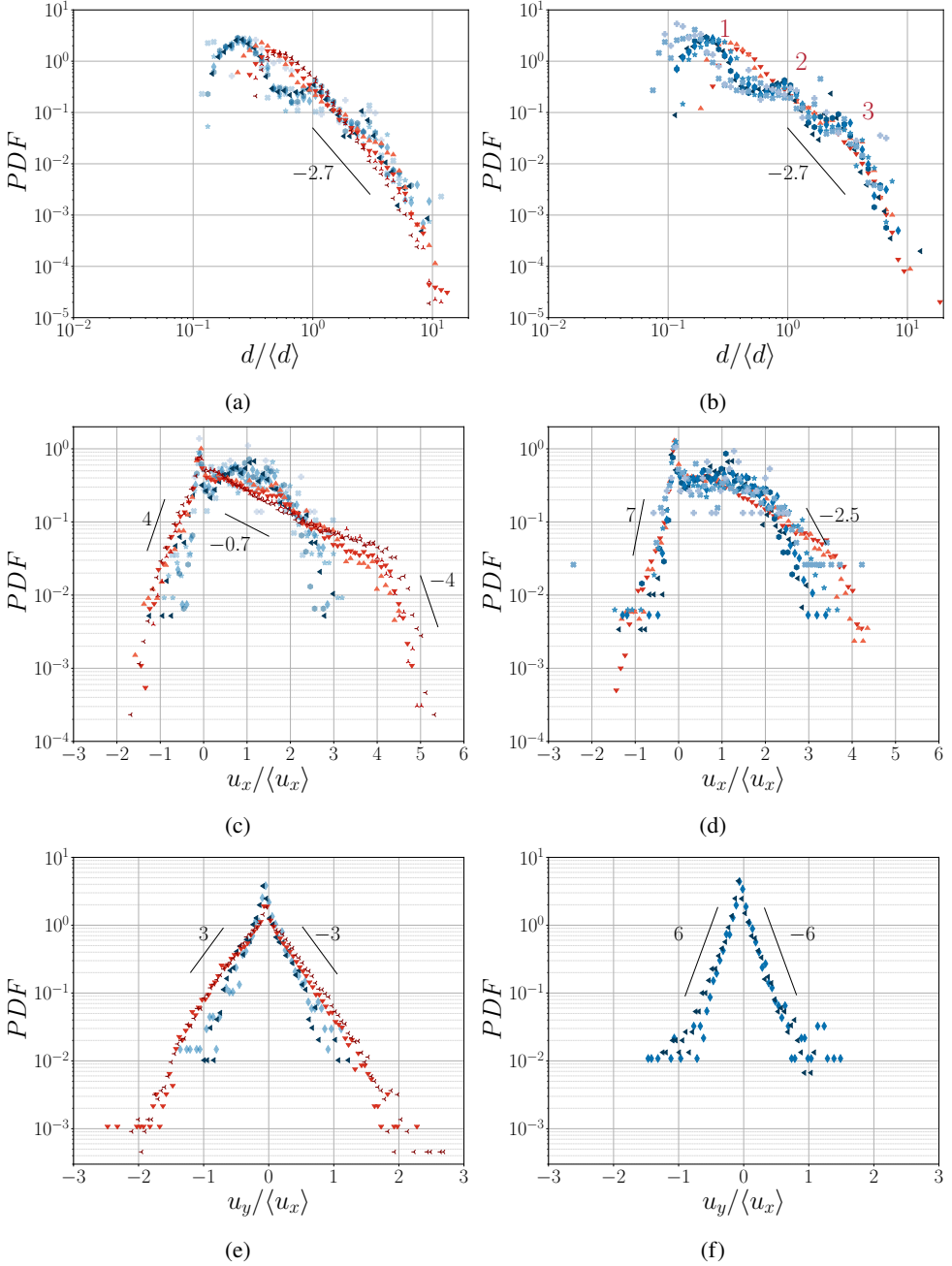


Figure 9: Distributions of $d/\langle d \rangle$ (a,b), $u_x/\langle u_x \rangle$ (c,d) and $u_y/\langle u_x \rangle$ (e,f) at $t/T_a = 15$ (left) and $t/T_a = 25$ (right). The blue and red colours denote the second wind-induced and atomisation regimes. The colour code denoting the DNS is the same as in Figure 3.

industrial jet shows a tail scaling as an exponential. Figure 10 gives the size distribution in a semi logarithmic scale. The time instant $t/T_a = 20$ has been chosen over $t/T_a = 25$ in order to highlight the trend of the size distribution in the second wind-induced regime thanks to the distribution for $We_2 = 73$ (DNS 7). It appears that, at both time instants, none of the size

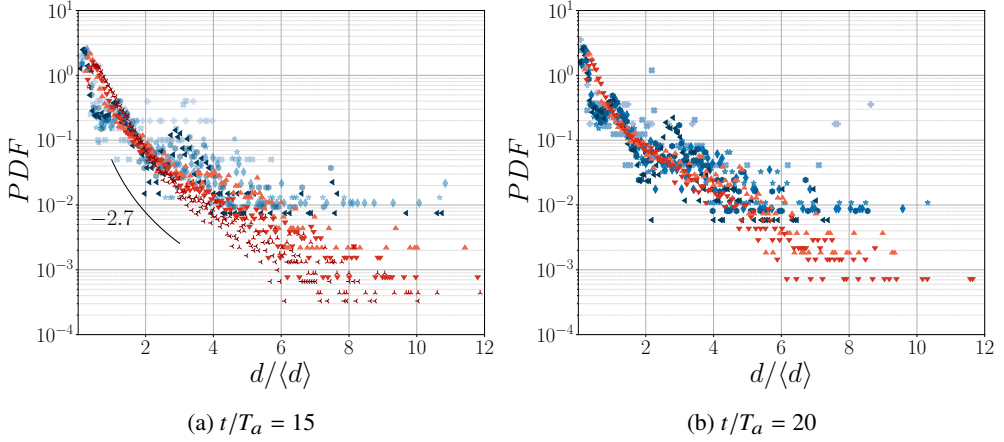


Figure 10: Distribution of $d/\langle d \rangle$ in semi-logarithmic scale at $t/T_a = 15$ and $t/T_a = 20$. The blue and red colours denote the second wind-induced and atomisation regimes, respectively. The colour code denoting the DNS is the same as in Figure 3. The solid black line corresponds to a power law of coefficient -2.7 , as in figure 9a and 9b.

distribution follows a unique exponential decay. Instead, the distribution in the atomisation regime follows two exponential scalings, the first one for $d/\langle d \rangle \in [0.5, 2]$ and the second one for $d/\langle d \rangle \in [4, 8]$, with a transition region scaling as $d/\langle d \rangle^{-2.7}$ for $d/\langle d \rangle \in [2, 4]$. Following the analysis of an experimental spray by Vallon (2021), the existence of those two scalings could indicate that the distribution is composed of two distributions originating from different fragmentation sources. The modelling of the size PDF by theoretical distributions is achieved in section 3.5.

Regarding the distribution of the axial velocity, it is often expected in jet fragmentation flows that the droplets show a positive axial velocity less than or equal to the injection velocity as they are globally advected towards increasing x/d_n . However, $\mathcal{P}_{u_x/\langle u_x \rangle}$ shows large probabilities for a range of negative velocities, $u_x/\langle u_x \rangle \in [-2, 0]$, with a sharp peak at $u_x/\langle u_x \rangle = 0$. The right-hand tail exists in both regimes on a range of velocities larger than the injection velocity U_{inj} . For instance, considering the droplet population for $We_2 = 40$ (DNS 6) lying in the second wind-induced regime at $t/T_a = 25$ with $\langle u_x \rangle = 1$ m/s, we have $\mathcal{P}(2 < u/\langle u_x \rangle < 3) > 0$, meaning that there exists droplets such that $u_x/U_{inj} \in [0.9, 1.35]$, thus being faster than the injection velocity $U_{inj} = 2.216$ m/s. The same conclusion can be drawn for the other DNS.

Surprisingly, for the atomisation regime, the tail expansions in the regions of negative velocities and velocities larger than U_{inj} follow a similar trend, scaling as $\exp(\pm a \times u_x/\langle u_x \rangle)$ with $a = 4$. However, in the second wind-induced regime, the left-hand tail and the right-hand tail present two different scalings: the former scales as $(u_x/\langle u_x \rangle)^7$ and the latter as $(u_x/\langle u_x \rangle)^{-2.5}$. The argument of the increasing relative velocity between the injection and the gas phase, and consequently in the standard deviation, can be considered to explain the difference in the tail expansion between the two regimes. Finally, in addition to the sharp peak for zero velocities, the axial velocity PDF is centered on $u_x/\langle u_x \rangle = 1$ in the second wind-induced regime and presents a continuous decrease scaling as $\exp(-0.7 \times u_x/\langle u_x \rangle)$ in the atomisation regime. The specific characteristics of the velocity PDF, $u_x < 0$ and $u_x \geq U_{inj}$, are explored in section 4.1.

3.5. Modeling the droplet size PDF

When it comes to modeling the distribution of the droplet size, one theoretical distribution is necessary to test: the Γ law derived from the ligament-mediated fragmentation framework (Villermaux 2020) along with its refinement exposed by Kooij *et al.* (2018), here after denoted f_Γ and $f_{\Gamma B}$. While the former was specifically designed to describe the droplet size PDF resulting from the breakup of a ligament, the latter was designed to describe the size PDF resulting from the overall fragmentation of a jet. A previous study carried out by Vallon *et al.* (2021) highlighted the limits of those two distributions for modelling size PDF far away from the nozzle, $x/d_n \in [400, 800]$ in the context of agricultural like sprays, and the satisfying performance of the law derived by Novikov & Dommermuth (1997) in the framework of turbulence intermittency, denoted f_ϵ in the following. More details about each law and the related framework are given in Vallon *et al.* (2021). The three theoretical laws write as follows:

$$f_\Gamma : \mathcal{P}(x = d/\langle d \rangle) = \frac{n^n}{\Gamma(n)} x^{n-1} e^{-nx}, \quad (3.1)$$

$$f_{\Gamma B} : \mathcal{P}(x = d/\langle d \rangle) = \frac{2(mn)^{(m+n)/2} x^{(m+n)/1-1}}{\Gamma(m)\Gamma(n)} \mathcal{K}_{m-n}(2\sqrt{nm}x), \quad (3.2)$$

$$f_\epsilon : \mathcal{P}(y = -\ln(l/l_1)) = \frac{a^{3/2}}{\sqrt{2\pi}\sigma y^{3/2}} \exp\left\{-\frac{a}{2\sigma^2}(ay^{-1/2} - y^{1/2})^2\right\}, \quad y \geq 0. \quad (3.3)$$

In the expression of f_Γ , n represents the corrugations of a ligament before its breakup. The corrugations determine the size PDF resulting from the breakup (Villermaux *et al.* 2004). The same logic takes place in the expression of $f_{\Gamma B}$. Additionally, the ligaments can show a large variety of sizes in the flow. This variety is taken into account by m which sets the order of the ligament size distribution (Kooij *et al.* 2018). Finally, the expression is conditioned by the modified Bessel function of the second kind \mathcal{K} whose order is set by $m - n$. Regarding f_ϵ , Novikov & Dommermuth (1997) considered a cascade mechanism and the ratio between the initial size l_1 and the resulting size l of a fragmenting droplet, where $a = \langle y \rangle$ and $\sigma = \langle (y - a)^2 \rangle$. It is worth noting that, even if f_ϵ relies on the cascade concept initially derived by Richardson (1922) and used in the seminal papers of Kolmogorov (1941*a,b*), the infinitely divisible nature of this distribution ensures that it is at no point close to a logarithmic normal distribution resulting from the Central Limit Theorem.

A systematic fit campaign is carried out to test the three distributions. Details of the procedure are given in appendix F. Figure 11 gives the best fits produced by f_Γ , $f_{\Gamma B}$ and f_ϵ in both fragmentation regimes at the time instant $t/T_a = 15$ while Table 5 gives the corresponding final parameters and the square of the Pearson coefficient r^2 . Qualitatively, the three theoretical distributions capture well the size PDF in both regimes and describe with a good accuracy the right-hand tail on the available range of sizes. No relevant comment can be drawn about the left-hand tail as no physical droplet sizes are available in the DNS, see section 3.3, and this range was discarded in the fit procedure. The slight differences between the distributions mainly lie in the description of the main mode. In both regimes, f_ϵ performs slightly better in capturing the main mode and the short left-hand tail. Additionally, the manual fit of the PDF modes for the second wind-induced regime indicates the good performance of f_Γ to describe the mode separately. Quantitatively, the values of r^2 bring a sharp light on the performance of each theoretical distribution. For both regimes, the law exposed by Kooij *et al.* (2018) shows r^2 values the closest to 1 with a mean computed over the two better fits equal to 1.00025. Then follows the Γ law and the distribution derived

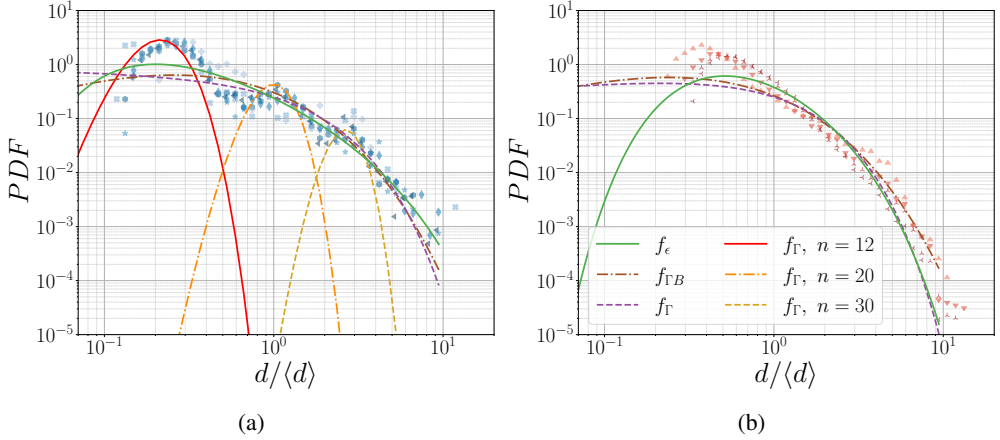


Figure 11: Color on-line. Fit of $\mathcal{P}_{d/\langle d \rangle}$ by f_{Γ} , $f_{\Gamma B}$ and f_{ϵ} in the second wind-induced regime (a) and the atomisation regime (b) at $t/T_a = 15$. The fit procedure is carried on the data shown here and the best fit is represented over $d/\langle d \rangle \in [10^{-2}, 20]$.

Regime	f_{Γ}			$f_{\Gamma B}$				f_{ϵ}			
	C	n	r^2	C	m	n	r^2	C	a	σ	r^2
SWI	0.704	0.932	0.919	0.741	2.513	2.513	0.998	0.751	0.921	1.111	0.829
ATO	0.594	1.269	0.930	0.660	2.411	2.411	1.007	0.670	1.058	0.670	0.927

Table 5: Final parameters and r^2 , truncated at the third decimal, for the best fits given by f_{Γ} , $f_{\Gamma B}$ and f_{ϵ} at $t/T_a = 15$. ATO: atomisation, SWI:second wind-induced. C is a prefactor applied to each function during the fit procedure.

by Novikov & Dommermuth (1997) with mean r^2 values respectively equal to 0.9245 and 0.878. Thus $f_{\Gamma B}$ better describes the size PDF in the flow, close to the nozzle, while f_{Γ} describes each mode separately. Meanwhile, f_{ϵ} shows a correct performance close to the nozzle, which achieves its good performance for describing multimodal size PDFs far away from the nozzle in the second wind-induced regime (Vallon *et al.* 2021).

4. Dynamics of the jet and the droplets: a two speed fragmentation

This section brings explanations about the specific features of the PDF of the droplet axial velocity, in connection with the vortex ring theory, and about the joint distribution of the droplet size and velocity. It also analyses the distribution of the droplets in the Reynolds - Ohnesorge phase space and compares it to experiments.

4.1. The axial velocity PDF and the jet head vortex ring

The analysis of the distribution of the axial velocity of the droplets in section 3.4 highlighted the existence of droplets showing negative velocities and velocities larger than U_{inj} , two infrequent features for a jet fragmentation. In order to investigate those two characteristics, it is interesting to have a glance on the spatial distribution of the droplets such that $u_x/U_{inj} < 0$ or $u_x/U_{inj} > 1$. To do so, the cylindrical coordinates $(x/d_n, r/d_n, \theta)$ are preferred to the Cartesian coordinates.

Figure 12 gives the spatial evolution in cylindrical coordinates of the probabilities

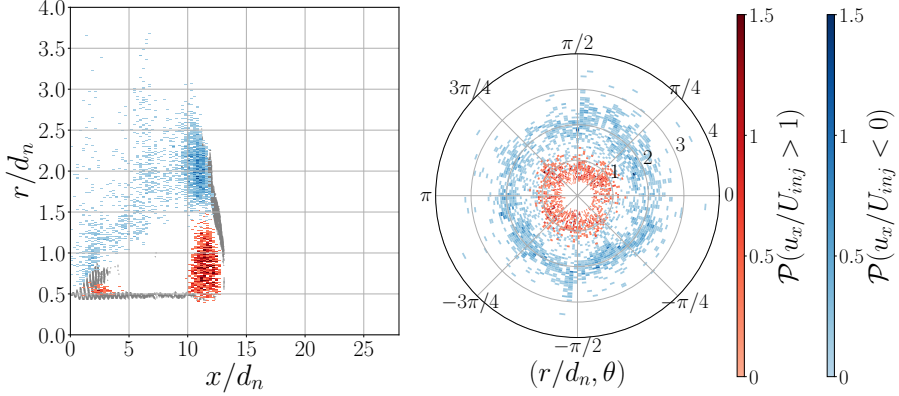


Figure 12: Spatial evolution of the probabilities $\mathcal{P}(u_x/U_{inj} < 0)$ and $\mathcal{P}(u_x/U_{inj} > 1)$ for $We_2 = 99.8$ (DNS 8) at $t/T_a = 15$ in cylindrical coordinates $(x/d_n, r/d_n, \theta)$. For each 2D graph, the probabilities are integrated on the third direction. On the $(x/d_n, r/d_n)$, the gray bullets represent the mean jet interface and few droplets, see appendix C for the details.

$\mathcal{P}(u_x/U_{inj} < 0)$ and $\mathcal{P}(u_x/U_{inj} > 1)$. For each 2D graph, the probabilities are integrated on the third direction, e.g. along the θ direction for the $(x/d_n, r/d_n)$ graph. Note that the liquid core starts at $r/d_n = 0.5$ and that the jet extends up to $x/d_n \approx 12.5$. In the $(x/d_n, r/d_n)$ space, the droplets appear to be located in four regions. The ones being faster than U_{inj} are preferentially located next to the nozzle ($0 < x/d_n < 0.5, r/d_n = 0.5$) and at the backside of the jet head up to half of the head sheet extension ($10 < x/d_n < 15, 0.5 < r/d_n < 1.5$). The former are due to the jet forcing. Indeed, the forcing described in section 2.3 is sinusoidal with a mean equal to U_{inj} and some droplets issued from the corolla fragmentation can show velocities larger than U_{inj} . The droplets showing negative velocities are preferentially located at the backside of the jet head from the half of the head extension up to its edge and located on a tail expanding over $x/d_n \in [0, 10]$ and $r/d_n \in [0.5, 2.5]$. The negative velocity or the velocity larger than U_{inj} of the droplets located at the downstream face of the jet head can be connected to the recirculation occurring behind it. Finally, the negative velocities along the tail towards $(x/d_n = 0, r/d_n = 0.5)$ can correspond to some droplets ejected from the recirculation region, with r/d_n increasing because of the increasing radius of the jet head in the time range $t/T_a \in [0, 15]$. The spatial distribution in the $(r/d_n, \theta)$ space shows homogeneity along the θ direction and a clear distinction between the two droplet groups along the r direction. The velocities larger than U_{inj} are concentrated in the boundary layer region, $r/d_n \in [0.5, 1]$, while the negative velocities spread over it, $r/d_n \in [1.5, 2.5]$.

Now that the droplets with, at first sight, unexpected axial velocities, $u_x/U_{inj} < 0$ and $u_x/U_{inj} > 1$, are located in the recirculation region behind the jet head, assessing this recirculation would help to explain why such velocities are reached. Looking at the distribution of u_x/U_{inj} is a time saver for this purpose, as it quantifies in a straightforward manner the range of velocities relatively to U_{inj} happening in this region. $\mathcal{P}_{u_x/U_{inj}}$ is given in Figure 13 and the ranges of unexpected velocities are $u_x/U_{inj} \in [-0.5, 0]$ and $u_x/U_{inj} \in [1, 1.5]$.

Assuming that the recirculation observed behind the jet head behaves as a vortex ring behind a plate, it is possible to use the developments of Saffman (1992) describing the dynamics of such unsteady objects to express the velocity at the vortex core u_c in terms of the plate velocity U_d , see appendix G:

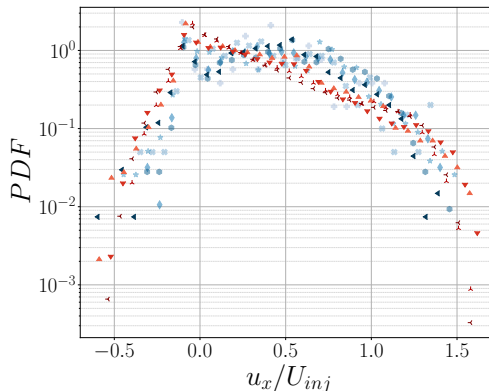


Figure 13: Distribution of u_x/U_{inj} at $t/Ta = 15$. The blue and red colours denote the second wind-induced and atomisation regimes. The colour code denoting the DNS is the same as in Figure 3.

$$u_c = \left(\frac{c}{R}\right)^{-1} \frac{2}{\pi^2 \sqrt{2/3}} U_d \quad (4.1)$$

where c and R are respectively the core radius and the vortex radius. For a uniform core $c/R = 0.19$, for a hollow core $c/R = 0.14$, leading to u_c respectively equal to $1.31 U_d$ and $1.77 U_d$. Taking $c/R = 0.165$, the mean value between 0.19 and 0.14, $u_c = 1.504 U_d$. In our flow, the jet head can be approximated as a disc behind which a vortex ring develops. In section 3, we observed that the jet head has the same velocity as U_{inj} , so $U_d = U_{inj}$. The velocity at the core edge then equals $\pm 1.5 U_{inj}$ and corresponds to the range of unexpected droplet velocities, $u_x/U_{inj} \in [-0.5, 0]$ and $u_x/U_{inj} \in [1, 1.5]$. Thus, the negative velocities and velocities larger than U_{inj} result from the vortex ring dynamics taking place at the downstream side of the jet head.

4.2. Joint distribution of the droplet size and axial velocity

The fragmentation of a jet or droplets is governed by aerodynamic and surface tension forces. Depending on the equilibrium between those, droplets of a given size and velocity result. Those two quantities influence each other comparably to a two-way coupling mechanism. Thus, looking at the joint distribution of the size and the axial velocity could bring extra information to the analysis of the marginal PDF $\mathcal{P}_{d/\langle d \rangle}$ and $\mathcal{P}_{u_x/\langle u_x \rangle}$. Figure 14 gives the joint distribution of $d/\langle d \rangle$ and $u_x/\langle u_x \rangle$ for $We_2 \in \{40, 130\}$ (DNS 6 and 9), respectively in the second wind-induced regime and the atomisation regime.

It is possible to recover the characteristics of the marginal PDF in the joint distributions. For instance, in the joint distribution for $We_2 = 40$ (DNS 6), three patches are noticeable along the size axis and correspond to the three modes of $\mathcal{P}_{d/\langle d \rangle}$, $d/\langle d \rangle \in \{0.2, 1, 2.5\}$. In addition, the negative velocities and velocities larger than U_{inj} described in section 3.4 and explained in section 4.1 are also noticeable. Observing so is expected as the marginal PDFs are simply the integration of the joint PDF on the size or the velocity axes.

In the second wind-induced regime, the negative axial velocities and the velocities larger than U_{inj} are preferentially observed for the first two size modes, while the third size mode is concentrated around ($d/\langle d \rangle = 2.5$, $u_x/\langle u_x \rangle \approx 1.5$) and the tail, from $d/\langle d \rangle \approx 3$ and towards large sizes, seems to be centered on $u_x/\langle u_x \rangle = 1$. Globally, the smaller droplets appear to have, at the same time, a dispersion being large along the velocity axis and being short

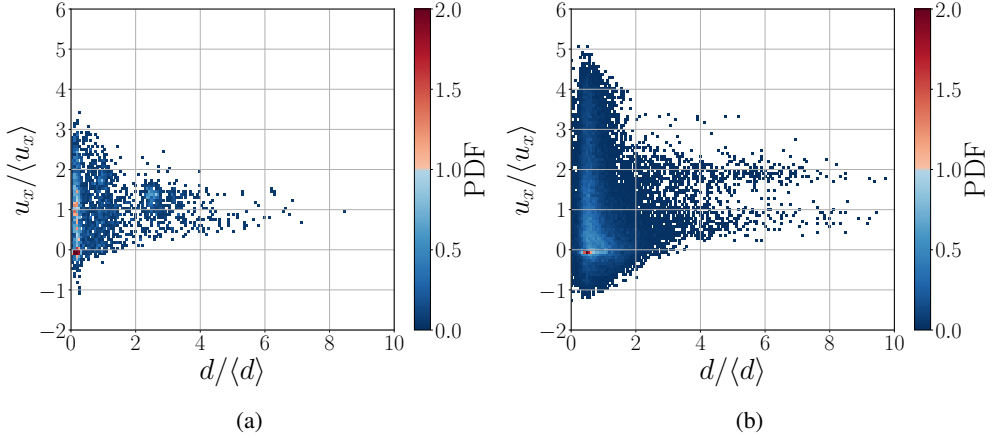


Figure 14: Joint distributions of the size and the axial velocity of the droplets for (a) $We_2 = 40$ (DNS 6) in second wind-induced regime at $t/T_a = 30$ and for (b) $We_2 = 130.3$ (DNS 9) in atomisation regime at $t/T_a = 15$.

on the size axis. Conversely, the larger droplets show a large dispersion along the size axis and a short one along the velocity axis. This corresponds to the literature and the common behaviors of tracers and ballistic objects which are classically observed. In comparison, even if tracers and ballistic objects are visible as well, the aspect of the joint distribution in the atomisation regime is different. Once again, the negative velocities and the velocities larger than U_{inj} are preferentially observed for the smaller droplets. However, the distribution shows two tails along the size axis, one centered on $u_x/\langle u_x \rangle \approx 0.75$ and the second one centered on $u_x/\langle u_x \rangle \approx 2$. Thus, the smaller and larger droplets still respectively behave like tracers and ballistic objects, but the ballistic objects show two traveling velocities. Conversely to the experimental observations (Vallon *et al.* 2021), the joint distributions do not show a clear elbow shape. Also, drawing a third group of droplets showing a similar dispersion along the size and velocity axes, as in the experimental analysis, seems less manifest here. Such a group could be extrapolated from the joint distribution and the second size mode, $d/\langle d \rangle = 1$, in the second wind-induced regime and for $d/\langle d \rangle \in [1.5, 2.5]$, while the velocity spans over $u_x/\langle u_x \rangle \in [0, 2]$ in both cases.

Similarly to section 4.1, it is possible to check out the spatial distribution of the droplets corresponding to the tails of the joint distribution $\mathcal{P}(d/\langle d \rangle, u_x/\langle u_x \rangle)$ for $We_2 = 130$ (DNS 9) in the atomisation regime. Those droplets are such that $d/\langle d \rangle > 4$ and are distinguished by their axial velocity being larger or smaller than $1.5\langle u_x \rangle$. Alike the PDF of the axial velocity of the droplets, the joint distribution shows the same feature for the larger droplets for all the DNS in the atomisation regime. Once again, it is more practical to express the conditions on the size and the velocity independently of the arithmetic average, but relatively to the injection conditions. Thus, the condition on the size writes as $d/d_n > 0.075$ and $0.4 U_{inj}$ is considered to be the threshold to distinguish the two tails. Figure 15 gives the spatial evolution in cylindrical coordinates of the probabilities $\mathcal{P}(d/d_n > 0.075, u_x/U_{inj} < 0.4)$ and $\mathcal{P}(d/d_n > 0.075, u_x/U_{inj} > 0.4)$. As for Figure 12, the liquid core starts at $r/d_n = 0.5$ and the jet extends up to $x/d_n \approx 12.5$. The droplets from each tail appear to exist in specific regions of the space. The large, fast droplets, $d/d_n > 0.075$ and $u_x/U_{inj} > 0.4$, are preferentially located in the boundary layer region, $r/d_n \in [0.5, 1]$, from the nozzle to the jet head. The large, slow droplets, for which $d/d_n > 0.075$ and $u_x/U_{inj} < 0.4$, are located on the downstream side of the jet head and around the maximal head sheet extension. The two

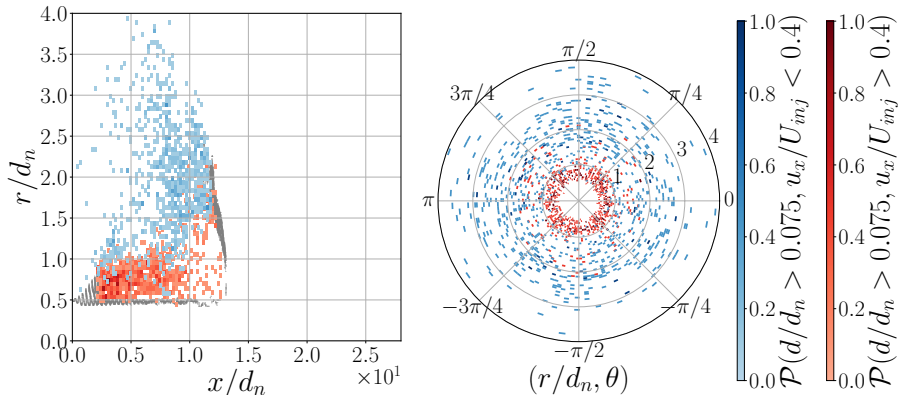


Figure 15: Spatial evolution of the probabilities $\mathcal{P}(d/d_n > 0.075, u_x/U_{inj} < 0.4)$ (blue) and $\mathcal{P}(d/d_n > 0.075, u_x/U_{inj} > 0.4)$ (red) for $We_2 = 99.8$ (DNS 8) at $t/T_a = 15$ in cylindrical coordinates. For each 2D graph, the probabilities are integrated on the third direction. On the $(x/d_n, r/d_n)$ graph, the gray boundary represents the mean jet interface and few droplets, see appendix C for the details.

groups show some overlapping in the recirculation region. It is possible that some droplets are caught in the vortex circulation, even if they preferentially behave as ballistic objects. In the $(r/d_n, \theta)$ space, the distributions are homogeneous along the azimuthal axis, which respects the flow symmetry, and the same distribution along the r/d_n -axis appears between the two groups. Thus, the two tails of the joint distribution of the size and the velocity come from the existence of two sources of fragmentation in the flow: the head sheet edge and the corollas developing from the jet forcing.

4.3. Governing parameters at the droplet scale

The joint distribution of the size and the axial velocity of the droplets gives some insights on the droplet dynamics in the flow. However, compared with the experiments, the numerical distributions show a slightly more complex trend and do not allow to characterise droplets with different behaviors on the basis of the marginal PDF characteristics. Beyond this, it would be interesting to have a glance on the flow perceived by a droplet as well as the droplet deformation resulting from the droplet-flow interaction. Without detailing the flow around each droplet down to the smallest scales, it is possible to characterise such a flow by considering its governing parameters, the particulate Reynolds number and the particulate Ohnesorge number, respectively expressed as:

$$Re_p = \frac{|u_{p,x} - U_{g,x}|d}{\nu_l}, \quad Oh_p = \frac{\mu_l}{\sqrt{\rho_l \sigma d}} \quad (4.2)$$

where d , $u_{p,x}$ and $|u_{p,x} - U_{g,x}|$ are the particle diameter, the particle axial velocity and its relative velocity compared to $U_{g,x}$, the x component of the gas phase velocity averaged over the domain. The particulate Reynolds number not only brings light on the balance between the inertial and viscosity forces at the scale of a droplet but it also brings information on the product of the droplet relative velocity and its diameter. By concatenating the size and the velocity of a droplet, the latter quantity could be seen as a potential of fragmentation. The higher the product $d \cdot |u_{p,x} - U_{g,x}|$ is, the more likely the droplet will fragment in multiple elements. It also enables to distinguish the droplet-flow interactions between droplets having the same size but different relative velocities or, equivalently, having the same relative

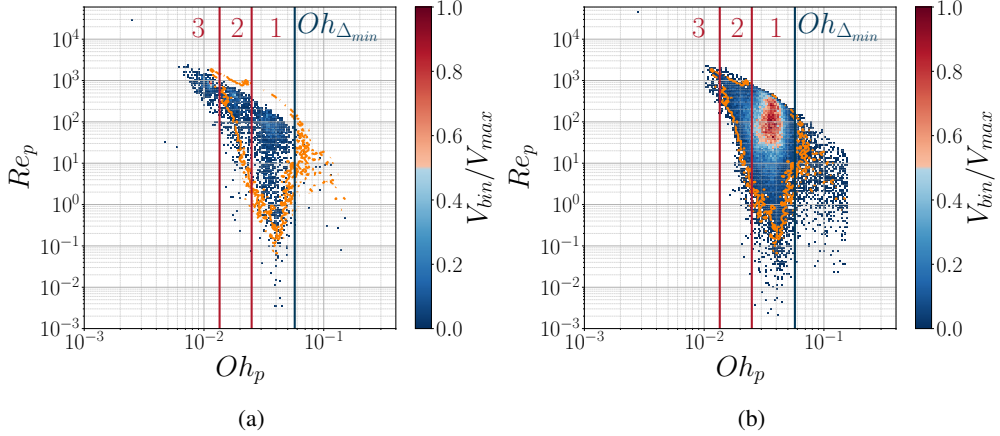


Figure 16: Joint volume histogram of Re_p and Oh_p for the droplet population for $We_2 = 40$ (DNS 6) at $t/T_a = 30$ (a) and for $We_2 = 165$ (DNS 10) at $t/T_a = 15$ (b). The Ohnesorge number corresponding to the smallest grid cell, $Oh_{\Delta_{min}}$, is indicated by the vertical blue line. The vertical red lines indicate the limits between the 3 modes of the size PDF for $We_2 = 40$ (DNS 6), figure 9b. The orange line represents the isovalue $V_{bin}/V_{max} = 0.03$ for $We_2 = 165$ (DNS 10).

velocity and different sizes. In addition, the particulate Ohnesorge number characterises the ratio between the viscosity forces and the product of the inertial and surface tension forces. This dimensionless number is usually used to characterise droplet deformation in a given flow. The larger is Oh_p , the less deformable is the droplet. Thus, even if they give global information on the droplet-scale flow, the combinations of Re_p and Oh_p could help to characterise the droplet behaviors depending on their possible deformation and potential of fragmentation. Figure 16 gives the normalised joint volume histogram of Re_p and Oh_p of the droplet population for $We_2 \in \{40, 165\}$ (DNS 6 and 10) respectively at $t/T_a = 30$ and $t/T_a = 15$. Note that the quantity which is plotted is the total volume of the droplets contained in a bin ($\Delta Re_p, \Delta Oh_p$), denoted V_{bin} , and normalised by the maximum value of V_{bin} , denoted V_{max} .

First of all, the Oh_p values larger than $Oh_{\Delta_{min}}$ correspond to the droplets smaller than the smallest cell size Δ_{min} and are not physically relevant. Considering the pair (Re_p, Oh_p) reshapes drastically the droplet data. Regarding $We_2 = 165$ (DNS 10), the two peaks present for the large sizes as well as the peaks around large velocities and negative velocities for the small sizes in figure 14 do not appear anymore in the joint volume histogram of the particulate dimensionless numbers. In addition, while the trends of the size-velocity joint distributions are significantly different between the two fragmentation regimes, the limits of the joint volume histogram appear not only to be regular but also follow similar trends between the two fragmentation regimes, as shown by the comparison of the joint histogram for $We_2 = 40$ (DNS 6) and the edge contour for $We_2 = 165$ (DNS 10). Regarding the histogram values, different modes appear in the joint histogram of each DNS. For the DNS 6, in the swi regime, it is possible to denote the three size modes, observed in section 3.4, denoted from 1 to 3 and separated at $Oh_p \in \{1.35 \times 10^{-2}, 2.5 \times 10^{-2}\}$ by the red vertical lines. Each droplet group shows some dispersion along the Re_p direction, dispersion which increases when the droplet size decreases. The population thus shows three subgroups whose dynamics seems to mainly be governed by their size. From those three size subgroups, only the modes 1 and 2 remain in the joint volume histogram of the DNS 10, in the atomisation regime. The mode of large sizes, mode 3, does not exist in the atomisation regime because

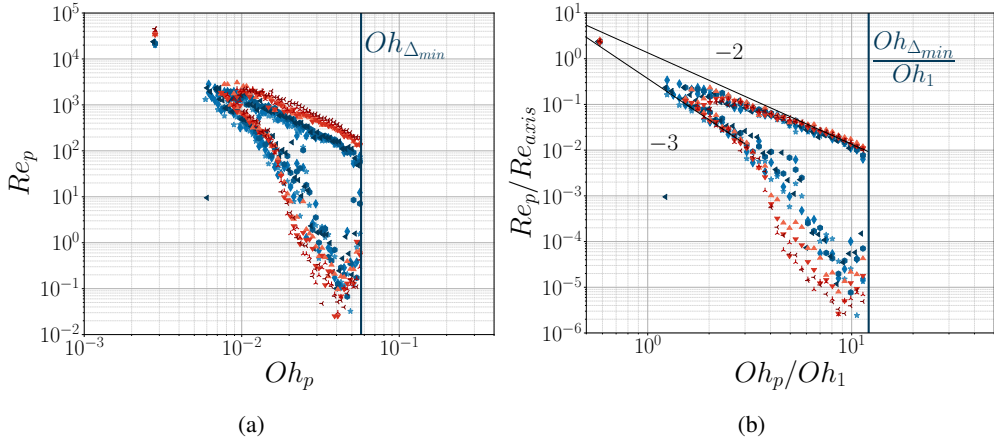


Figure 17: Color on-line. Edges of (a) the joint volume histograms and of (b) the normalised joint volume histograms at $t/T_a = 15$. The blue and red colours denote the second wind-induced and atomisation regimes. The colour code denoting the DNS is the same as in Figure 3.

the corolla issued from the forcing cannot develop nor create rim leading to the generation of such droplet sizes. For the latter DNS, the mode 1, existing at large Oh_p and indicated by the red region in figure 16b, gains in importance and is the main size mode in the atomisation regime, existing for $Oh_p \in [2.5, 5] \times 10^{-2}$ and $Re_p \in [30, 400]$. Additionally, the dispersion of the modes for moderate and small Oh_p increases between the two regimes while respecting the similar outer limits, as the droplet data spread over all the space delimited by the edge contour for $We_2 = 165$ (DNS 10). Finally, it is worth noting the absence of droplets in the region of large particulate Reynolds and small particulate Ohnesorge, $(Re_p, Oh_p) \in ([10^3, 10^4], [1, 7] \times 10^{-3})$, i.e. droplets whose size and axial velocity are of the order of d_n and U_{inj} .

The comparison of the edge contour for $We_2 = 165$ (DNS 10) with the joint volume histogram for $We_2 = 40$ (DNS 6) given by figure 16 suggests that the joint histograms follow similar borders regardless of the fragmentation regime. Figure 17 dives in a more detailed comparison of the joint histogram borders by superposing the edges for all the DNS and proposes a normalisation of the two dimensionless numbers. The edges are obtained by sampling each joint histogram along the Oh_p direction and keeping for each sample the maximum of the ordinates and the ordinate of the percentile at 7%. This technique enables to discard the outlier points existing at small Re_p . From the edges of the non normalised joint histograms, it appears clearly that the joint histograms evolve in the same phase space for both fragmentation regimes and that the borders only show a slight evolution with the gaseous Weber number We_2 . Note that the isolated points in the top left corner are the Re_p and Oh_p values corresponding to the liquid core. Those points depart from Re_1 and Oh_1 because the liquid core has a volume larger than that of a sphere of diameter d_n . As a reminder, the injection dimensionless numbers are given in Table 2.

In order to normalise Re_p and Oh_p , one can choose the Reynolds number on the jet axis Re_{axis} , computed with the nozzle diameter d_n and $u_{x,axis}$ the jet velocity on the x -axis, and the injection Ohnesorge number Oh_1 computed with d_n . In our simulation, the velocity of the jet along the x -axis does not show any diminution, thus $u_{x,axis} = U_{inj}$ and $Re_{axis} = Re_1$. Making the distinction between the injection velocity and the jet velocity on the axis might appear auxiliary here but is relevant for comparing the numerical data with experiments.

Once normalised, all the upper and lower borders of the joint histograms collapse. Not only those borders collapse but also show a power law dependency. For $Re_p/Re_{axis} \geq 10^{-2}$, the former scales such that $Re_p/Re_{axis} = 1.35(Oh_p/Oh_1)^{-2}$ and the latter scales such that $Re_p/Re_{axis} = 0.37(Oh_p/Oh_1)^{-3}$. The collapse however does not hold for the borders on the range $Oh_p/Oh_1 \in [4, 10]$ and $Re_p/Re_{axis} \leq 10^{-2}$, which could simply result from the difference in the relative velocity and the extreme values along the Re_p -axis. Additionally, not only the isolated points corresponding to the liquid core collapse, but also they lie within the space delimited by the two power laws. Thus, a spray developing after the pinching region, in the same configuration, could show a phase space delimited by the same power laws and spreading from the liquid core towards the smallest droplets. Finally, as all the contours collapse in figure 17b, it is possible to add that this cascade in the phase space ($Re_p/Re_{axis}, Oh_p/Oh_1$) is independent of the gaseous weber number We_2 .

Overall, the comparison of the joint volume histogram in the second wind-induced regime, $We_2 = 40$ (DNS 6), and in the atomisation regime, $We_2 = 165$ (DNS 10), indicates that the dominant modes of the droplet population evolve with We_2 . Particularly, the mode for small Oh_p , i.e. large droplet sizes, does not exist in the atomisation regime. Also, the atomisation regime presents a larger dispersion in Oh_p and Re_p . This is expected as the increase in We_2 creates aerodynamic conditions in which large droplets are very unlikely to survive, or even be generated, and the increase of the relative velocity between the gas and the liquid induces an increase of the deviation of the size and the axial velocity, see section 3.4. This analysis highlights the possibility to reshape the size and velocity data of the droplets into a regular shape, even if the size-velocity joint distribution shows irregular boundaries and infrequent features. Additionally, it indicates that the joint histogram values of the particulate dimensionless numbers evolve with We_2 while respecting outer borders which are largely independent of We_2 . Normalising the particulate dimensionless numbers by the injection dimensionless numbers shows that the droplets exist over a steady phase space, delimited by power and exponential laws. Finally, such joint volume histogram opens the way for qualifying the different flow regimes undergone by the droplets and the consequent fragmentation mechanisms.

4.4. Droplet phase space: simulations and experiments

Vallon *et al.* (2021) proposed, among others, a detailed analysis of the experimental joint distribution of the size and axial velocity of the droplets in the case of a water jet injected into quiescent air at $We_2 = 24$ and lying in the second wind-induced regime. The experimental apparatus used to perform simultaneous measurements of the size and the velocity of the droplets is detailed by Felis *et al.* (2020). The originality of that experimental campaign lies in the simultaneity of the DTV size-velocity measurements and the distance where they were carried out: from 400 to 800 nozzle diameters along the jet axis. Complementarily, and following the insights of section 4.3, it is possible to look at the experimental joint volume histogram of the particulate Reynolds and Ohnesorge numbers. Figure 18 gives the joint volume histogram for Re_p/Re_{axis} and Oh_p/Oh_1 derived from the experimental measurements of Felis *et al.* (2020). Note that the mean velocity of the liquid phase on the jet axis $u_{x,axis}$ is no longer equal to the injection velocity, $U_{inj} = 35$ m/s, but has decreased by 20% at $x/d_n = 800$.

Once again, the borders of the joint volume histogram are well-defined and can be easily modelled. The upper and lower borders split into two scalings. For $Re_p/Re_{axis} \geq O(10^{-3})$, the borders follow a power law while they follow an exponential scaling for smaller values of Re_p/Re_{axis} . The upper and lower borders are respectively denoted \mathcal{B}_{up} and \mathcal{B}_{low} and their scaling is such that:

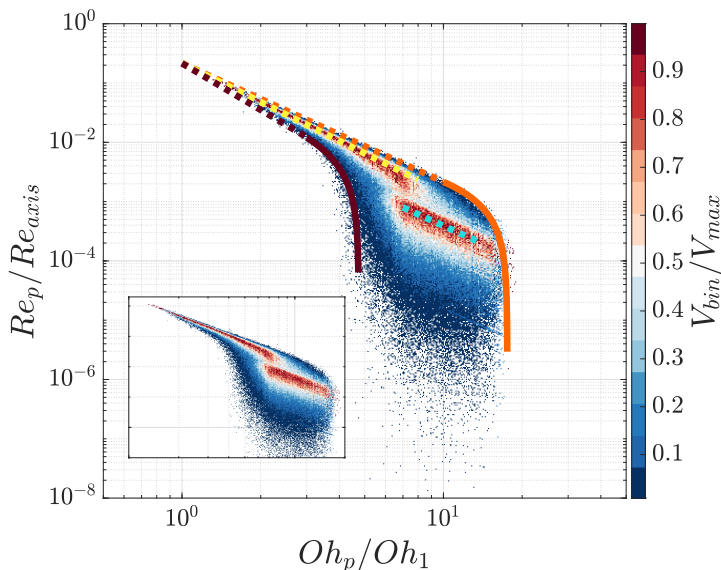


Figure 18: Experimental joint volume histogram of Re_p/Re_{axis} and Oh_p/Oh_1 at $x/d_n = 800$. The dash-dot lines represent the power law scalings while the solid lines represent the exponential scalings. The insert recalls the joint volume histogram without the modelled borders.

$$\mathcal{B}_{up} : \begin{cases} \frac{Re_p}{Re_{axis}} = 0.215 \left(\frac{Oh_p}{Oh_1} \right)^{-2}, & \forall Oh_p/Oh_1 \in [1, 10] \\ \frac{Re_p}{Re_{axis}} = \exp \left(-0.1 \left(\frac{Oh_p}{Oh_1} + 45.1 \right) \right) - 1.90 \times 10^{-3}, & \forall Oh_p/Oh_1 \in [10, 20] \end{cases} \quad (4.3)$$

$$\mathcal{B}_{low} : \begin{cases} \frac{Re_p}{Re_{axis}} = 0.215 \left(\frac{Oh_p}{Oh_1} \right)^{-2.61}, & \forall Oh_p/Oh_1 \in [1, 3] \\ \frac{Re_p}{Re_{axis}} = \exp \left(-0.6 \left(\frac{Oh_p}{Oh_1} + 3.65 \right) \right) - 6.5 \times 10^{-3}, & \forall Oh_p/Oh_1 \in [3, 5] \end{cases} \quad (4.4)$$

Note that, for a given value of Oh_p , the upper border describes the fastest droplets at a given size while, for a given value of Re_p , it describes the smallest droplets at a given velocity. Thus, the upper border can be seen as the border describing the smallest and fastest droplets in a given region of the phase space, the reverse logic holds for the lower border. Additionally, two main “paths” can be distinguished in the joint histogram. The first one lies in the power law region and the second one in the exponential region, respectively denoted \mathcal{P}_1 and \mathcal{P}_2 , both of them follow a power law scaling such that:

$$\begin{aligned} \mathcal{P}_1 : \frac{Re_p}{Re_{axis}} &= 0.215 \left(\frac{Oh_p}{Oh_1} \right)^{-2.175}, & \forall Oh_p/Oh_1 \in [1, 7] \\ \mathcal{P}_2 : \frac{Re_p}{Re_{axis}} &= 0.039 \left(\frac{Oh_p}{Oh_1} \right)^{-2}, & \forall Oh_p/Oh_1 \in [7, 14] \end{aligned} \quad (4.5)$$

Let us focus on the borders scaling as a power law. Starting from the expression of Oh_p , it is possible to rewrite Re_p as $Re_p = \sigma^{-1} \mu_l |u_{p,x} - U_{g,x}| Oh_p^{-2}$. Knowing that in this region $Re_p = C Oh_p^{-2-\alpha}$ with $C \in \mathbb{R}$, we then have $|u_{p,x} - U_{g,x}| = \sigma C Oh_p^{-\alpha}$, which is equivalent

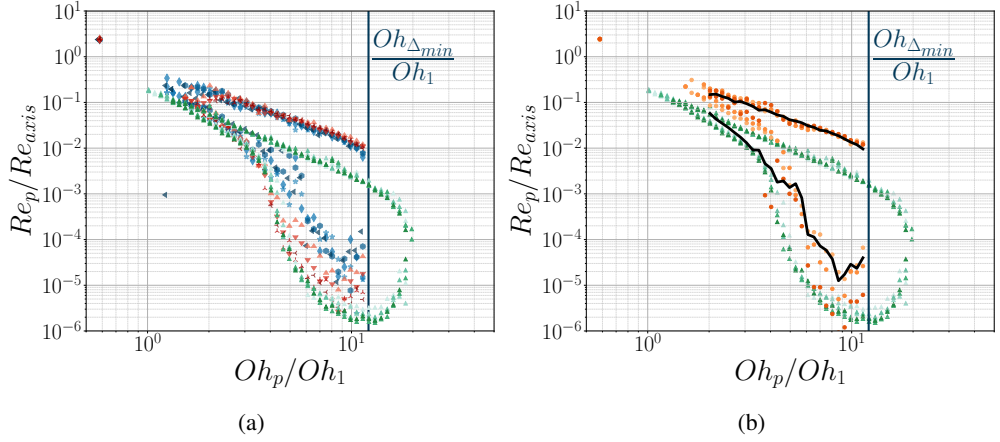


Figure 19: Color on-line. Comparison of the borders of the joint volume histograms obtained from the DNS campaign and from the experimental data of Felis *et al.* (2020). The blue and red colours denote the second wind-induced and atomisation regimes. The color code denoting the DNS is the same as in Figure 3. The green triangles represent the experimental data and the orange bullets represent DNS with $U_{inj} = 2.216\text{m/s}$ and different density ratios, $\rho_1/\rho_2 = 82.5, 110, 165$. In (b), the black solid line indicates the mean value of the numerical joint histogram edges for $We_2 \in [26, 165]$ (blue and red).

to $|u_{p,x} - U_{g,x}| \propto d^{\alpha/2}$. The droplets then show a velocity relative to the gas phase which increases with the droplet size. The coefficient α necessarily lies in \mathbb{R}^+ . Indeed, a negative α would mean that the relative velocity of a droplet decreases when its size increases and consequently that larger objects would be more sensitive to the gas phase flow, which goes against the observation of ballistic objects in fragmentation flows. Consequently, the borders scaling as Oh^{-2} seem to result from dynamical limits. Regarding the lower border scaling as a power law, we have $\alpha \in \{0.4, 0.45, 0.5, 0.56, 0.61\}$ for $x/d_n \in \{400, 500, 600, 700, 800\}$. Inferring a rule on the evolution of the upper bound of α from the experimental data seems reckless.

Regarding the exponential scaling of the borders, it is interesting to note the existence of an offset along Oh_p and Re_p . The droplets being on the upper border preferentially have a smaller size and a larger relative velocity, while those on the lower border have a larger size and a smaller relative velocity. In order to have all the droplets lying in a stable configuration, which corresponds to the region where $Re_p < O(10^{-3})$, the difference in the droplet dynamics has to be accounted for. This is what the offsets along Oh_p and Re_p in the exponential scaling enable to do.

Figure 19a compares the edge contour of the experimental and numerical joint volume histograms. When comparing the original experimental histograms and the numerical ones, it appears that the phase spaces in which the droplets evolve show ranges of existence being very similar between the experiments and the simulations. Even if an offset along the Re_p/Re_{axis} -axis exists, they lie in the same Oh_p/Oh_1 range. By multiplying the edge contour of the experimental joint volume histogram by 3, the edges of the numerical and the experimental data collapse. Thus, we have $(Re_p/Re_{axis})_{num} = C \times (Re_p/Re_{axis})_{exp}$, where $C \approx 3$, which leads to:

$$\frac{|u_{p,x} - U_{g,x}|_{num} d_{num}}{|u_{p,x} - U_{g,x}|_{exp} d_{exp}} = C \frac{d_{n,num} \times u_{x,axis,num}}{d_{n,exp} \times u_{x,axis,exp}} \quad (4.6)$$

and results to

$$|u_{p,x} - U_{g,x}|_{num} d_{num} \approx 1.8 |u_{p,x} - U_{g,x}|_{exp} d_{exp} \quad (4.7)$$

with $u_{x,axis,exp} = 0.8 \times U_{inj,exp} = 28$ m/s and $u_{x,axis,num} = U_{inj,num} = 4.5$ m/s. The numerical and experimental contours lie in the same range of Oh_p/Oh_1 . Thus, it can be assumed that $d_{exp}/d_{n,exp} \approx d_{num}/d_{n,num}$ which implies:

$$\frac{d_{num}}{d_{exp}} \approx 3.73, \quad \frac{|u_{p,x} - U_{g,x}|_{num}}{|u_{p,x} - U_{g,x}|_{exp}} \approx 0.48. \quad (4.8)$$

The experimental and numerical mean sizes are respectively $\langle d \rangle_{exp} = 95 \mu\text{m}$, averaged over the 5 x/d_n positions, and $\langle d \rangle_{num} \approx 300 \mu\text{m}$, at $t/T_a = 34$ in the second wind-induced regime. The ratio of the means equals 3.16, thus $\langle d \rangle_{num}/\langle d \rangle_{exp} \approx d_{num}/d_{exp}$ and verifies the previous result.

Explaining why the last three ratios appear, Eqs. 4.7 and 4.8, must be made carefully. On the one hand, the way the measurements of the size and the velocity of the droplets is carried out greatly differs between the experiments and the simulations. In the simulations, once a droplet is detected thanks to the tag function of Basilisk, see section 2.2, its volume and velocity are computed as the volume average in 3D of the cell values contained in the droplet. In the experiments, the measurements of the droplet size and velocity are carried out with a 2D laser sheet thanks to DTV. In addition, the measurement of the mean gas phase velocity also differs. While numerically it results from the velocity average over all the cells in the gas phase, the experimental mean gas phase velocity is estimated from LDV measurements at different radial positions and then averaged along those positions. On the other hand, it is important to keep in mind that the experimental and numerical data correspond to two drastically different physical spaces. The former were measured for $x/d_n = 800$ and the latter for $x/d_n \approx 20$.

With these limits in mind, different hypotheses can be sketched. As the measurements are carried in two drastically different regions of the fragmenting jet, the three ratios could reveal some dynamics occurring at the overall jet scale, for instance the overall slowdown of the droplet population when the droplet spray moves towards larger x/d_n . If it was the case, it could be expected that the edges of the experimental joint volume histograms would be translated towards smaller Re_p/Re_{axis} , see Figure 19a, as they span over a distance of 400 d_n . But, no such translation is noticeable for the experimental edges.

The difference along the Re_p -axis between the experimental and numerical joint histograms could also raise from the difference of the density ratios considered in the simulations and experiments. Indeed, since gravity is not considered, the effects of density are accounted by the Reynolds and Ohnesorge numbers. Figure 19b gives the evolution of the joint histogram edges obtained for 3 density ratios, $\rho_l/\rho_g \in \{82.5, 110, 165\}$, such that $We_2 = 40$, see appendix H. These density ratios remain small compared to experimental values, $O(1000)$ for water injected in air, but are already quite computationally expensive. No translation of the joint histogram edges towards smaller Re_p/Re_{axis} values is noticeable, thus discarding this hypothesis too. The choice of the normalisation for the Reynolds number could also be an explanation. Using the Reynolds number computed over d_n and the averaged velocity of the dispersed liquid phase, instead of u_{axis} , could help to make the edges of the joint volume histograms collapse, both experimentally and numerically.

Notwithstanding those limitations and differences, it still seems legitimate to conclude that the joint histogram edges are self similar. This conclusion only holds for the edges and not for the joint histogram values, which evolve very differently between the experiments and the simulations.

Yet, the two jet flows differ in terms of fragmentation mechanisms. In the experimental

flow, the bag breakup fragmentation plays an important role while it is totally absent in the numerical flows. In the experiments, the droplets undergoing bag breakup originate from the liquid core pinch and are characterised by a large size and axial velocity. As the liquid core is still developing in the simulations, the absence of such droplets is expected. Even if the joint histogram edges are self similar, they slightly differ for large values of particulate Reynolds and Ohnesorge numbers where the experimental joint histograms exhibit a well-defined tail. Besides, section 3.5 shows that the ligament-mediated fragmentation describes well the droplet fragmentation in the numerical flows. Thus, it is tempting to conclude that the droplets are likely to undergo a bag breakup fragmentation when $Oh_p/Oh_1 < 2$ and a ligament mediated fragmentation when $Oh_p/Oh_1 \geq 2$.

5. Conclusion

In this work, the droplet population generated by the fragmentation of a round jet in a quiescent gas medium was studied numerically for different gaseous Weber numbers We_2 spanning the second wind-induced regime and part of the atomisation regime. At first, the statistical moments of the size, the axial velocity and the radial velocity were depicted and their evolution with We_2 was detailed. The study of the distribution of the droplet size shows the existence of three modes in the second wind-induced regime, while only one mode exists in the atomisation regime. Complementary, the size distribution shows two exponential decays connected by a transition region scaling as a power law. In this near-field (close to the nozzle) fragmentation, the size distribution is better modelled by the law derived by Kooij *et al.* (2018) in the context of ligament-mediated fragmentation than by the law derived by Novikov & Dommermuth (1997) in the framework of turbulence intermittency. This could, at first sight, raise from the difference in the fragmentation mechanisms occurring in the region close to the nozzle, studied here, and the region far away from the nozzle studied in Vallon (2021). On the side of the axial velocity distribution, additionally to elucidating the scaling of the axial velocity distribution tails, the origin of the droplet velocities being negative and larger than the injection velocity U_{inj} is explained thanks to the vortex ring theory of Saffman (1992), vortex ring which sustains the recirculation region on the downstream side of the jet head. The existence of a double tail along the size direction for the size-velocity joint distribution is also explained by spatially separating the droplets evolving in the boundary layer and those ejected from the jet head.

The analysis also scaled down to the flow perceived by the droplets with the study of the droplet volume histogram over the phase space of the particulate Reynolds and Ohnesorge numbers. Properly scaled by the injection Ohnesorge number Oh_1 and the Reynolds number computed on the jet axis Re_{axis} , the boundaries of the joint volume histograms from the DNS collapse, thus indicating the weak dependence of the joint histogram boundaries on the gaseous Weber number. The collapse is also obtained between the numerical and the experimental joint volume histograms, with a slight correction along the Reynolds axis for the far-field experimental one. This highlights the existence of a phase space properly bounded which contains the whole droplet population as well as the jet liquid core. Advantages could be taken from this result for modeling the turbulent jet fragmentation in terms of particulate dimensionless numbers or for improving the model of mass transfer proposed by Vallon (2021). Overall, the good accuracy of the statistical properties of the droplet population with the theoretical models, as well as with the experimental data, validate the accuracy of the simulations within the numerical limitations.

Further work could be done regarding the droplet dynamics and geometry. Now that the interface of the jet and the droplet population are described, it could be possible to focus on the size distribution resulting from specific fragmentation mechanisms, like the fragmentation

of the rims in the second wind-induced regime. This could help to understand the origin of the 3 modes observed for the size distribution in this regime. Also, performing a Lagrangian tracking of the rims in the DNS lying in the second wind-induced regime would enable to verify the break-up of such toroidal ligaments and compare the resulting size distribution with the Γ distribution from the ligament-mediated fragmentation theory. Finally, a statistical analysis of the ligament geometry in the atomisation regime, specifically in the DNS with the highest We_2 , could help to better describe the ligament size and corrugation distributions over the jet fragmentation.

Acknowledgments. This work was granted access to the HPC resources of CINES under the allocation 2019-A0072B11103 made by GENCI.

Funding. This research received no specific grant from any funding agency, commercial or not-for-profit sectors.

Declaration of interests. The authors report no conflict of interest.

Author ORCIDs.

R. Vallon, <https://orcid.org/0000-0003-0770-787X>;

M. Abid, <https://orcid.org/0000-0002-0438-4182>;

F. Anselmet, <https://orcid.org/0000-0001-6443-7437>

Author contributions. R.V. performed the direct numerical simulations, developed the data analysis scripts, carried most of the data analysis and wrote the manuscript. M.A. provided scientific and technical supervisions, including key insights regarding the fragmentation and vortex theories. F.A. provided scientific supervision. F.A. and M.A. contributed equally to designing the work and proofreading the manuscript. All authors contributed equally to reaching conclusions.

Appendix A. Computation of the most unstable mode

Following the work of Yang (1992) on the growth of waves in round jets, it is possible to characterise the most unstable axisymmetric mode. The author studied the stability of an infinitesimal perturbation on the surface of a round jet of radius a . The configuration is the same as described in 2.3. Additionally, the gas phase can be injected at a velocity U_2 and the fluids are incompressible and inviscid. In this section, the injection velocity previously denoted U_{inj} is denoted U_1 .

The velocity and pressure fields can be split into an averaged part and a fluctuation part: $\mathbf{u}_i = \mathbf{U}_i + \mathbf{u}'_i$ and $p_i = P_i + p'_i$, where $i \in \{1, 2\}$ respectively denotes the liquid and gaseous phases. Injecting this decomposition into the governing equations, expressed in cylindrical coordinates (r, θ, z) , and applying the divergence operator gives the pressure disturbance equation :

$$\nabla^2 p'_i = 0, \quad \nabla^2 = \frac{1}{r} \frac{\partial}{\partial r} r \frac{\partial}{\partial r} + \frac{1}{r^2} \frac{\partial^2}{\partial \theta^2} + \frac{\partial^2}{\partial z^2} \quad (\text{A } 1)$$

Assuming a 3D disturbance with a normalised wavelength number ka and m in the streamwise and azimuthal directions, the perturbed quantities are $p'_i = p'_i(r) e^{i(kz+m\theta)+\alpha_{tg}t}$ and $\mathbf{u}'_i = \mathbf{u}'_i(r) e^{i(kz+m\theta)+\alpha_{tg}t}$, where α_{tg} is the temporal growth rate and m introduces the non axisymmetric variations of the disturbance. Eq. A 1 then becomes:

$$\left(\frac{1}{r} \frac{\partial}{\partial r} r \frac{\partial}{\partial r} - \frac{m^2}{r^2} - k^2 \right) p_i(r) = 0 \quad (\text{A } 2)$$

Resolving this equation gives a solution for $p_i(r)$, Eq. A 3, depending on the first and second type modified Bessel functions of order m , respectively denoted I_m and K_m . This solution can be used with the mass conservation equation for the linearised perturbation to derive a solution for \mathbf{u}'_i , Eq. A 4.

$$p_i(r) = C_{i,1} I_m(kr) + C_{i,2} K_m(kr) \quad (\text{A } 3)$$

$$\mathbf{u}'_i = - \frac{\nabla (p_i(r) e^{i(kz+m\theta)+\alpha_{tg}t})}{\rho_i (\alpha_{tg} + ikU_i)} \quad (\text{A } 4)$$

where the four constants $C_{i,1}$ and $C_{i,2}$ have to be derived regarding the boundary conditions. The pressure is finite in the liquid at $r = 0$ and in the gas when $r \rightarrow +\infty$, thus $C_{1,2} = C_{2,1} = 0$. Let η_1 and η_2 denote the perturbed displacements of the interface and Δp_σ the pressure jump due to the surface tension σ . The pressure follows $\Delta p_\sigma = \sigma(1/R_1 + 1/R_2)$ with R_1 and R_2 the principal radii of curvature. The remaining two constants can be derived from the pressure jump, $p_1 - p_2 = \Delta p_\sigma$, and the interface displacement, $\eta_1 = \eta_2$. The perturbed displacements satisfy:

$$v_i = \frac{\partial \eta_i}{\partial t} + U_i \frac{\partial \eta_i}{\partial x} \quad (\text{A } 5)$$

with v_i the velocity component in the radial direction. By letting $\eta = \eta_1 = \eta_2 = \eta_0 e^{i(kz+m\theta)+\alpha_{tg}t}$, Yang (1992) showed that to the first order of η , $1/R_1 + 1/R_2 = 1/d_n - 1/d_n^2 [1 - m^2 - (ka)^2] \eta_0$. The continuity equations then become:

$$C_{11} \left(I_m(ka) - \frac{\sigma [1 - m^2 - (ka)^2]}{a^2} \frac{I'_m(ka)}{\rho_1 (\alpha_{tg} + ikU_1)^2} \right) - C_{22} K_m(ka) = 0 \quad (\text{A } 6)$$

DNS	C_{tot} (10^6)	$\overline{V_{num}}$ (10^6 cells/s)	t_{max}/T_a	$L_{j,max}/d_n$	N_{tot}
1	4.43	0.59	34	28	70
2	29.29	0.93	34	28	459
3	53.83	2.23	34	28	1949
4	42.15	1.96	34	28	2182
5	51.41	1.73	34	28	2448
6	34.13	1.92	34	28	3545
7	77.45	2.46	24.2	21.5	9725
8	105.6	2.59	20.0	17.0	18,478
9	141.7	2.59	17.5	14.4	32922
10	154.4	2.56	16.5	14.2	45046

Table 6: Numerical performances.

$$C_{11} \frac{I'_m(ka)}{\rho_1(\alpha_{tg} + ikU_1)^2} - C_{22} \frac{K'_m(ka)}{\rho_2(\alpha_{tg} + ikU_2)^2} = 0 \quad (\text{A } 7)$$

The latter equation system admits a non-trivial solution when its determinant is zero. This condition gives the following dispersion equation:

$$(\rho_{1m} + \rho_{2m})\alpha_{tg}^2 + 2ik\alpha_{tg}(\rho_{2m}U_2 + \rho_{1m}U_1) - k^2(\rho_{2m}U_2^2 + \rho_{1m}U_1^2) - \frac{k\sigma}{a^2} [1 - m^2 - (ka)^2] = 0 \quad (\text{A } 8)$$

with:

$$\left\{ \begin{array}{l} \rho_{1m} = \gamma_m \rho_1 \\ \rho_{2m} = \beta_m \rho_2 \\ \gamma_m = kI_m(ka)/I'_m(ka) \\ \beta_m = -kK_m(ka)/K'_m(ka) \\ I'_m(ka) = \left. \frac{dI_m(kr)}{dr} \right|_{r=a} \\ K'_m(ka) = \left. \frac{dK_m(kr)}{dr} \right|_{r=a} \end{array} \right. \quad (\text{A } 9)$$

The dispersion equation, Eq. A 8, is a quadratic equation in α_{tg} and the expression of the nondimensional temporal growth rate for the m -th transversal mode can be derived from it:

$$(\alpha_r^*)_m^2 = \frac{\gamma_m \beta_m Q \cdot (ka)^2}{(\gamma_m + \beta_m Q)^2} + \frac{ka}{We} \frac{1 - m^2 - (ka)^2}{\gamma_m + \beta_m Q} \quad (\text{A } 10)$$

where $(\alpha_r^*)_m^2 = (\alpha_r)_m^2 / [(U_1 - U_2)^2 / d_n^2]$, $We = [d_n(U_1 - U_2)\rho_1] / \sigma$ and $Q = \rho_2 / \rho_1$.

Appendix B. Numerical performances of the DNS

The computational performances can be tracked by checking the total number of cells used for each DNS, C_{tot} , the mean numerical velocity, $\overline{V_{num}}$, the maximal physical time, t_{max}/T_a , the maximum jet elongation, $L_{j,max}/d_n$ and the total number of detected droplets, N_{tot} . Table 6 summarizes the related numerical performances. All the DNS are split into 3 runs and were computed on the Occigen HPC (CINES, France).

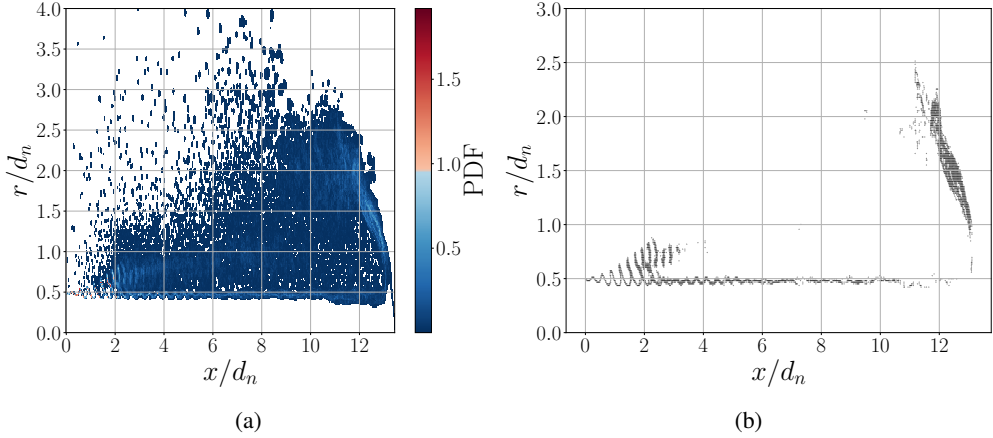


Figure 20: Joint distribution of the interface points in the $(x/d_n, r/d_n)$ space for $We_2 = 99.8$ (DNS 8) at $t/T_a = 15$ (a) and the interface filtered with a threshold of 0.2 (b).

Appendix C. Computation of the mean interface of the jet

Computing the mean interface of the jet is not straightforward and requires some processing. To extract it, it is first necessary to compute the joint distribution of the interface points in the physical space $(x/d_n, r/d_n)$. Once computed, the mean interface can be extracted from the distribution by filtering out the most probable interface points. This extraction step however relies on the choice of a threshold. This threshold can be empirically chosen such that it enables to depict the mean interface while discarding most of the interface related to the droplets.

Figures 20a and 20b respectively give the joint distribution of the interface points across the $(x/d_n, r/d_n)$ space and the interface filtered from the joint distribution with a threshold of 0.2, i.e. the interface points with a probability larger than 0.2. A way to refine the mean interface of the jet would be to consider the interface of the liquid core only, instead of considering all the interface points in the jet, i.e. the liquid core and all the droplets. The droplets would be then naturally discarded and the resulting interface would depict more precisely the mean interface around the jet head. Even so, the method used here is satisfactory for the following analysis.

Appendix D. Temporal evolution of the mean values of the size, axial velocity and radial velocity

Figure 21 gives the temporal evolution of the mean values of the size, the axial velocity and the radial velocity. Regarding the size and the axial velocity, after reaching a peak value for $t/T_a \in [5, 10]$, the mean values increase relatively steadily within the time scope under consideration. The time evolution of the mean of each DNS can be rescaled with We_2 . On one side, the mean size scaled by $We_2^{0.6}$ seems to evolve linearly with t/T_a . On the other side, it is possible to collapse the time evolution of the mean axial velocity for each regime by considering $\langle u_x \rangle We_2^{-1}$ for the second wind-induced regime and $\langle u_x \rangle We_2^{-0.3}$ for the atomisation regime. The evolution of u_y is specific in the sense that the flow is statistically axisymmetric and $\langle u_y \rangle$ should naturally be set to zero, which is verified here asymptotically. Due to the flow symmetry, the mean of u_z behaves the same as the one of u_y . The standard deviations, not shown here, reach a steady state faster than the mean values for the size and the velocities.

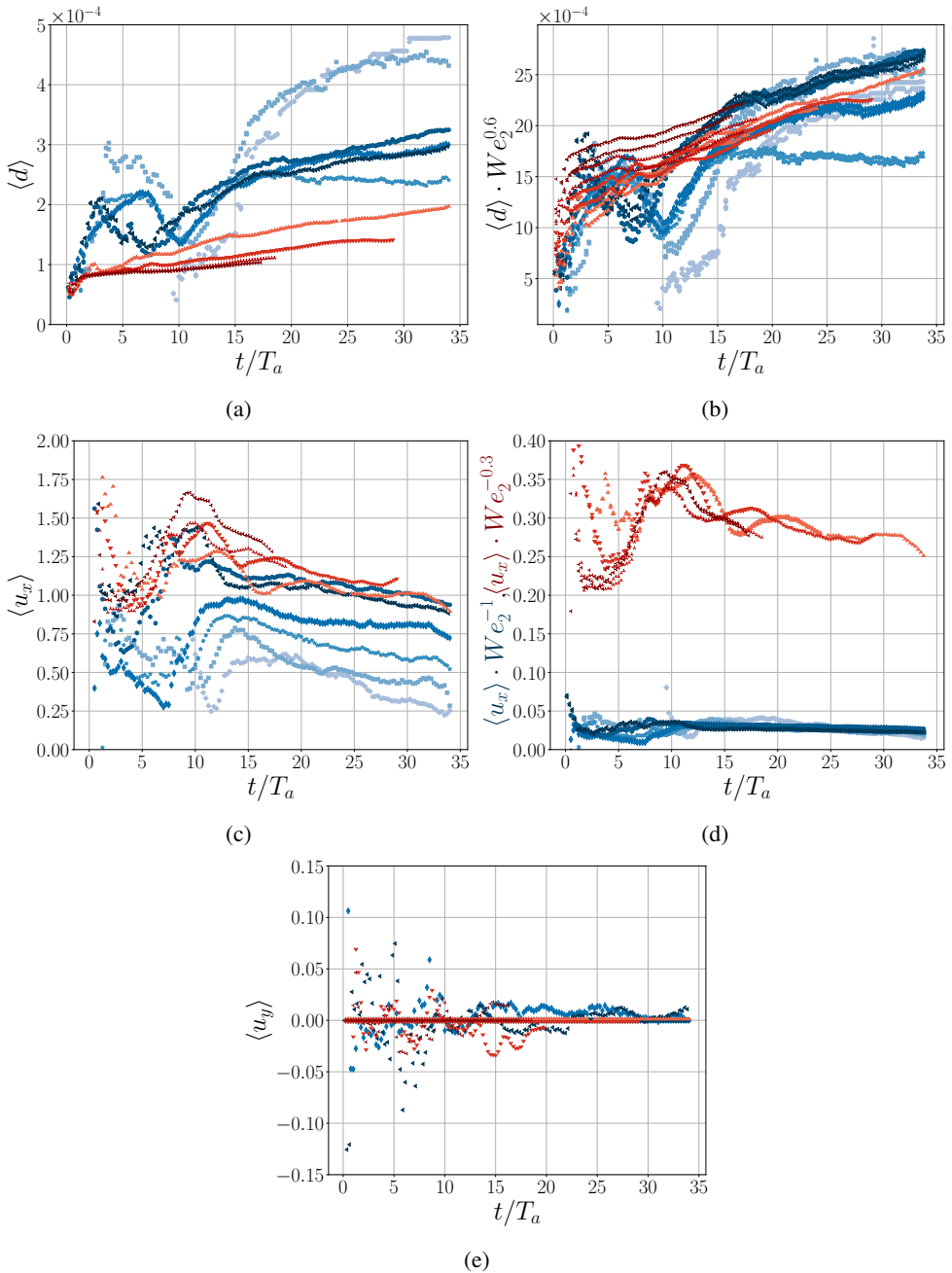


Figure 21: Temporal evolution of the mean $\langle \cdot \rangle$, unscaled (left) and scaled by We_2 (right) of the droplet size d (a,b), the axial velocity u_x (c,d) and the transverse velocity u_y (e). The units of the variables are the SI base units.

Appendix E. Evolution of the velocity statistical moments with We_2

Regarding the distribution of u_x , all the four statistical moments increase with We_2 . The increase in the mean and standard deviation indicates that the droplets are accelerated with We_2 , which is obvious as U_{inj} increases meanwhile, and that the dispersion in terms of

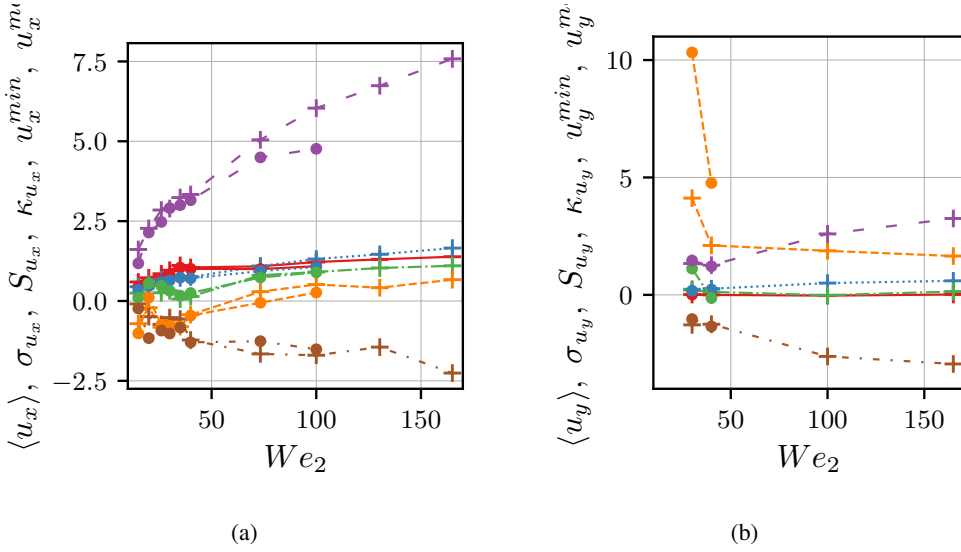


Figure 22: Evolution of $\langle \cdot \rangle$ (red), σ (blue), S (green), κ (orange), the minimum (purple) and maximum (brown) against We_2 for the axial velocity u_x (a) and the transversal velocity u_y (b). The pluses (+) correspond to $t/T_a = 15$ and the bullets (●) to $t/T_a = 25$. Note that S and κ are both dimensionless and that the dimensional variables are expressed with the SI base units.

velocity is larger, which also seems natural as the relative velocity between the injection and the gas phase velocity increases too. The same observation holds to explain the evolution of u_x^{max} and u_x^{min} . Concurrently, the skewness is positive and increases with We_2 , thus the axial velocity distribution is right-tailed with an increasing asymmetry. Compared to the skewness of the size distribution, the skewness of the distribution of u_x is much smaller and the distribution should be moderately skewed. Finally, the excess kurtosis not only increases but also changes sign for $We_2 \in [40, 70]$. The second wind-induced regime is then characterised by a negative excess kurtosis, which indicates tails being shorter and a peak being flatter than the ones of the Normal distribution. Conversely, the excess kurtosis in the atomisation regime, for the values of We_2 under consideration, is positive, indicating larger tails and a sharper peak compared to the Normal distribution. Furthermore, the excess kurtosis is smaller than 3 and the distribution has tails shorter than the ones of the Gaussian distribution. Thus, each fragmentation regime shows a characteristic tail spanning for the distribution of u_x .

The interpretation of the evolution of the statistical moments for the distribution of u_y is straightforward. As discussed previously, the statistical axisymmetry of the flow enforces a zero mean value as well as a symmetric distribution of u_y around its mean, i.e. a zero skewness. Those two consequences of the flow symmetry are verified for each We_2 value and highlighted by the evolution of u_y^{min} and u_y^{max} . Similarly to the distribution of u_x , the standard deviation increases with the gaseous Weber number because of the increasing relative velocity between the liquid injection and the gas phase and thus the shear. The excess kurtosis, the one subtracted by 3, remains stable and is positive. This indicates a steady behavior and tails being larger than those of the Gaussian distribution.

Appendix F. Systematic fit campaign for testing the theoretical size distributions

The systematic fit campaign carried out to test the three distributions uses the fitting algorithm of the EZYFIT toolbox developed by Moisy (2020) on MATLAB. This algorithm is said to be able to capture a given signal with a reference function when the parameters are set with initial values of the same order as the final values. Thus, the space of initial values has to be explored sufficiently to ensure that the optimum set of parameter values is captured for each theoretical distribution. To do so, the fit campaign is performed in two phases. In the first phase, 23 combinations of initial values are explored in linear and logarithmic modes, i.e. fitting the signal or its logarithmic transform. In the second phase, the best fits in each fitting mode and at the two time instants $t/T_a = \{15, 25\}$ are selected and tested a second time in order to improve the fit quality. Even if $\mathcal{P}_{d/\langle d \rangle}$ shows several modes in the second wind-induced regime, the fit of the size distribution is carried out for the main mode only, i.e. with only one theoretical distribution at a time. Finally, each theoretical PDF is weighted by a coefficient C which is let free in the fitting algorithm. Generally speaking, a fit shows a good agreement with a given signal when the Pearson coefficient r is close to 1. One can also use r^2 as a more discriminating criterion.

Appendix G. Vortex ring dynamics, deriving the velocity at the edge of the vortex core

Assuming that the recirculation observed behind the jet head behaves as a vortex ring behind a plate, it is possible to use the developments of Saffman (1992) which describe the dynamics of such unsteady objects. Let us consider a disc of radius a moving at a velocity U_d in the direction normal to the disc surface, denoted x hereafter, a vortex ring can develop on the downstream face and the velocity potential ϕ on the upstream face follows:

$$\phi = \mp \frac{2U_d}{\pi} \sqrt{a^2 - r^2}, \quad x = \pm 0, \quad y^2 + z^2 = r^2 < a^2 \quad (\text{G } 1)$$

If the disc dissolves, the vortex ring remains with a strength $\kappa(r) = 4U_d/\pi \times r/\sqrt{a^2 - r^2}$ and a vorticity $\omega = \kappa\theta\delta(x)$. The amplitudes of the hydrodynamic impulse $\dagger I$ in the x direction and the kinetic energy E are thus:

$$I = \frac{1}{2} \int (\mathbf{x} \times \omega)_x dV = \frac{1}{2} \int_0^a 2\pi r^2 \kappa dr = 8U_d a^3 / 3 \quad (\text{G } 2)$$

$$E = \frac{1}{2} \int \phi \frac{\partial \phi}{\partial n} dS = 4U_d^2 a^3 / 3 \quad (\text{G } 3)$$

In addition, the circulation Γ containing the disc while starting and ending at the disc center is such that:

$$\Gamma = \int_0^a \kappa dr = [\phi]_{r=0} = 4U_d a / \pi \quad (\text{G } 4)$$

Let us denote the vortex radius and the vortex core radius R and c and assume the conservation of the ring circulation and the hydrodynamic impulse. Knowing that the hydrodynamic impulse equals $\Gamma\pi R^2$ (Taylor 1953), the combination of Eqs. G 2 and G 4 results in $R =$

\dagger The concept of hydrodynamic impulse has a long history in theoretical hydrodynamics having been described by Lamb (1932). The advantage of the theory of hydrodynamic impulse is that it describes the physical origin of hydrodynamic forces and moments in terms of the vorticity generated at the body surface and its subsequent position in the fluid volume (Holloway & Jeans 2020).

DNS	U_{inj} (m/s)	ρ_2 (kg/m ³)	We_2	Re_1	f (kHz)	St
11	2.714	1/82.5	40	12159	0.918	1.52
12	3.134	1/110	40	14040	0.915	1.31
13	3.838	1/165	40	17195	0.911	1.06

Table 7: Injection velocities, gaseous density and corresponding gas Weber and liquid Reynolds numbers along with the frequency f of the most unstable mode and the corresponding forcing Strouhal number St .

$\sqrt{2/3}a$. Further calculations give the expression of the vortex ring velocity U_{vr} and of its energy depending on Γ , R and c :

$$U_{vr} = \frac{\Gamma}{4\pi R} \left[\log\left(\frac{8R}{c}\right) - \frac{1}{2} + \int_0^c \left(\frac{\Gamma(s)}{\Gamma}\right)^2 \frac{ds}{s} + o\left(\frac{c}{R}\right) \right] \quad (\text{G } 5)$$

$$E = \frac{1}{2}\Gamma^2 R \left[\log\left(\frac{8R}{c}\right) - 2 + \int_0^c \left(\frac{\Gamma(s)}{\Gamma}\right)^2 \frac{ds}{s} + o\left(\frac{c}{R}\right) \right] \quad (\text{G } 6)$$

Combining the latter two equations with Eq. G 3 enables to express the ratio of the vortex ring velocity U_{vr} along x and the disc velocity U_d :

$$\frac{U_{vr}}{U_d} = \frac{1}{4} + \frac{1}{\pi^2} \left(\frac{3}{2}\right)^{3/2} = 0.44 \quad (\text{G } 7)$$

The question of the velocity at the edge of the vortex core remains and is of most importance as it sets the droplet motion in the recirculation region. For a uniform core, c/R equals 0.19 while it equals 0.14 in the case of a hollow core. The velocity at the core edge, denoted u_c , can be expressed as a function of the circulation Γ , $u_c = \Gamma/2\pi c$. Using the expression of Γ given in Eq. G 4 and $R = \sqrt{2/3}a$, u_c rewrites as:

$$u_c = \left(\frac{c}{R}\right)^{-1} \frac{2}{\pi^2 \sqrt{2/3}} U_d \quad (\text{G } 8)$$

Appendix H. Large density-ratio DNS

The comparison of the edges of the experimental and numerical joint volume histogram over the space ($Oh_p/Oh_1, Re_p/Re_{axis}$), given in Figure 19a indicates a discrepancy along Re_p/Re_{axis} . In order to figure out if this discrepancy is due to the difference in the density ratio, several DNS with larger density ratio were ran. The gaseous Weber number is set to 40, as for the DNS 6. Except for ρ_2 , the parameters given by Table 1 are kept the same. Table 7 gives the injection velocity, ρ_2 , the corresponding We_2 and Re_1 along with the frequency f of the most unstable mode and the forcing Strouhal number St .

REFERENCES

- ABU-AL-SAUD, M. O, POPINET, S. & TCHELEPI, H. 2018 A conservative and well-balanced surface tension model. *Journal of Computational Physics* **371**, 896–913.
- AGBAGLAH, G., DELAUX, S., FUSTER, D., HOEPPFNER, J., JOSSERAND, C., POPINET, S., RAY, P., SCARDOVELLI, R. & ZALESKI, S. 2011 Parallel simulation of multiphase flows using octree adaptivity and the volume-of-fluid method. *Comptes Rendus Mécanique* **339**, 194–207.
- BELL, J. B., COLELLA, P. & GLAZ, H. M. 1989 A second-order projection method for the incompressible navier-stokes equations. *Journal of Computational Physics* **85** (2), 257–283.
- CHAUSSONNET, G., BRAUN, S., DAUCH, T., KELLER, M., KADEN, J., JAKOBS, T., SCHWITZKE, C., KOCH, R. & BAUER, H. 2018 Three-dimensional SPH simulation of a twin-fluid atomizer operating at high pressure. In *Proceedings of the 14th International Conference on Liquid Atomization & Spray Systems*. Chicago, IL, USA.
- CULICK, F. E. C. 1960 Comments on a ruptured soap film. *Journal of Applied Physics* **31**, 1128–1129.
- FAETH, G.M, HSIANG, L.-P & WU, P.-K 1995 Structure and breakup properties of sprays. *International Journal of Multiphase Flow* **21**, 99–127.
- FELIS, F., TOMAS, S., VALLET, A., AMIELH, M. & ANSELMET, F. 2020 Experimental analysis of the flow characteristics of a pressure-atomized spray. *International Journal of Heat and Fluid Flow* **85**, 108624.
- FUSTER, D., AGBAGLAH, G., JOSSERAND, C., POPINET, S. & ZALESKI, S. 2009 Numerical simulation of droplets, bubbles and waves: State of the art. *Fluid Dynamics Research* **41** (6), 065001.
- GOROKHOVSKI, M. & HERRMANN, M. 2008 Modeling primary atomization. *Annual Review of Fluid Mechanics* **40** (1), 343–366.
- HINZE, J. O. 1955 Fundamentals of the hydrodynamic mechanism of splitting in dispersion processes. *AIChE Journal* **1** (3), 289–295.
- HOLLOWAY, A.G.L. & JEANS, T.L. 2020 Hydrodynamic impulse generated by slender bodies in viscous flow. *Ocean Engineering* **206**, 106951.
- KOLMOGOROV, A. N. 1941a Energy dissipation in locally isotropic turbulence. *Doklady Akademii Nauk SSSR* **32**, 19–21.
- KOLMOGOROV, A. N. 1941b The local structure of turbulence in an incompressible fluid for very large Reynolds numbers. *Doklady Akademii Nauk SSSR* **30**, 301–303.
- KOOIJ, S., SIJS, R., DENN, M. M., VILLERMAUX, E. & BONN, D. 2018 What determines the drop size in sprays? *Physical Review X* **8** (3), 031019.
- LAGRÉE, P.-Y., STARON, L. & POPINET, S. 2011 The granular column collapse as a continuum: Validity of a two-dimensional Navier–Stokes model with a $\mu(I)$ -rheology. *Journal of Fluid Mechanics* **686**, 378–408.
- LAMB, H. 1932 *Hydrodynamics*, sixth edn. New York, NY, USA: DoverPublications.
- LEFEBVRE, A. H. & McDONELL, V. G. 2017 *Atomization and Sprays*, 2nd edn. CRC Press, Taylor & Francis.
- LING, Y., FUSTER, D., ZALESKI, S. & TRYGGVASON, G. 2017a Spray formation in a quasiplanar gas-liquid mixing layer at moderate density ratios: A numerical closeup. *Physical Review Fluids* **2** (1), 014005.
- LING, Y., LEGROS, G., POPINET, S. & ZALESKI, S. 2017b Direct numerical simulation of an atomizing biodiesel jet: Impact of fuel properties on atomization characteristics. In *Proceedings ILASS–Europe 2017. 28th Conference on Liquid Atomization and Spray Systems*. Universitat Politècnica València.
- LÒPEZ-HERRERA, J.M., GAÑÁN-CALVO, A.M., POPINET, S. & HERRADA, M.A. 2015 Electrokinetic effects in the breakup of electrified jets: A Volume-Of-Fluid numerical study. *International Journal of Multiphase Flow* **71**, 14–22.
- MOISY, F. 2020 EzyFit 2.44. The MathWorks, Inc.
- NOVIKOV, E. A. 1994 Infinitely divisible distributions in turbulence. *Physical Review E* **50** (5), R3303–R3305.
- NOVIKOV, E. A. & DOMMERMUTH, D. G. 1997 Distribution of droplets in a turbulent spray. *Physical Review E* **56** (5), 5479–5482.
- POPINET, S. 2003 Gerris: A tree-based adaptive solver for the incompressible Euler equations in complex geometries. *Journal of Computational Physics* **190** (2), 572–600.
- POPINET, S. 2015 A quadtree-adaptive multigrid solver for the Serre–Green–Naghdi equations. *Journal of Computational Physics* **302**, 336–358.
- POPINET, S. 2018 Numerical Models of Surface Tension. *Annual Review of Fluid Mechanics* **50** (1), 49–75.
- POPINET, S. & COLLABORATORS 2013 Basilisk. <http://www.basilisk.fr/>.
- POPINET, S. & COLLABORATORS 2016 Basilsik-Atomisation. www.basilisk.fr/src/examples/atomisation.c.

- RICHARDSON, L. F. 1922 *Weather Prediction by Numerical Process*. Cambridge, UK: Cambridge University Press.
- SAFFMAN, P. G. 1992 *Vortex Dynamics*. Cambridge, UK: Cambridge University Press.
- SIMMONS, H. C. 1977 The correlation of drop-size distributions in fuel nozzle sprays. Part II. The drop-size/number distribution. *Journal of Engineering for Gas Turbines and Power* **99** (3), 315–319.
- STEVENIN, C., TOMAS, S., VALLET, A., AMIELH, M. & ANSELMET, F. 2016 Flow characteristics of a large-size pressure-atomized spray using DTV. *International Journal of Multiphase Flow* **84**, 264–278.
- TAYLOR, G. I. 1953 Formation of a vortex ring by giving an impulse to a circular disk and then dissolving it away. *Journal of Applied Physics* **24** (1), 104.
- TAYLOR, G. I. 1959 The dynamics of thin sheets of fluid III. Desintegration of fluid sheets. *Proceedings of the Royal Society A* **253**, 313–321.
- TENNEKES, H. & LUMLEY, J. L. 1972 *A First Course in Turbulence*. Cambridge, MA, US & London, UK: MIT Press.
- TRYGGVASON, G., SCARDOVELLI, R. & ZALESKI, S. 2011 *Direct Numerical Simulations of Gas-Liquid Multiphase Flows*. Cambridge, UK: Cambridge University Press.
- VALLON, ROMAIN 2021 Liquid jet atomisation: Statistical analysis in the close field and in the far field. PhD thesis, Aix-Marseille Université, IRPHE, Marseille.
- VALLON, R., ABID, M. & ANSELMET, F. 2021 Multimodal distributions of agricultural-like sprays: A statistical analysis of drop population from a pressure-atomized spray. *Physical Review Fluids* **6** (2), 023606.
- VAN HOOFT, J. A., POPINET, S., VAN HEERWAARDEN, C. C., VAN DER LINDEN, S. J. A., DE ROODE, S. R. & VAN DE WIEL, B. J. H. 2018 Towards adaptive grids for atmospheric boundary-layer simulations. *Boundary-Layer Meteorology* **167** (3), 421–443.
- VILLERMAUX, E. 2020 Fragmentation versus Cohesion. *Journal of Fluid Mechanics* **898**, P1.
- VILLERMAUX, E., MARMOTTANT, P. G. M. & DUPLAT, J. 2004 Ligament-mediated spray formation. *Physical Review Letters* **92** (7), 074501.
- YANG, H. Q. 1992 Asymmetric instability of a liquid jet. *Physics of Fluids A: Fluid Dynamics* **4**, 681–689.
- ZANDIAN, A., SIRIGNANO, W. A. & HUSSAIN, F. 2017 Planar liquid jet: Early deformation and atomization cascades. *Physics of Fluids* **29** (6), 062109.
- ZHANG, B., POPINET, S. & LING, Y. 2020 Modeling and detailed numerical simulation of the primary breakup of a gasoline surrogate jet under non-evaporative operating conditions. *International Journal of Multiphase Flow* **130**, 103362.